JCB Journal of Cell Biology

ARTICLE

TRIM37 prevents formation of condensate-organized ectopic spindle poles to ensure mitotic fidelity

Franz Meitinger[1,2,3*], Dong Kong[4*], Midori Ohta[1,2,3*], Arshad Desai[1,2,3**], Karen Oegema[1,2,3**], and Jadranka Loncarek[4**]

Centrosomes are composed of a centriolar core surrounded by pericentriolar material that nucleates microtubules. The ubiquitin ligase TRIM37 localizes to centrosomes, but its centrosomal roles are not yet defined. We show that TRIM37 does not control centriole duplication, structure, or the ability of centrioles to form cilia but instead prevents assembly of an ectopic centrobin-scaffolded structured condensate that forms by budding off of centrosomes. In ∼25% of TRIM37-deficient cells, the condensate organizes an ectopic spindle pole, recruiting other centrosomal proteins and acquiring microtubule nucleation capacity during mitotic entry. Ectopic spindle pole–associated transient multipolarity and multipolar segregation in TRIM37-deficient cells are suppressed by removing centrobin, which interacts with and is ubiquitinated by TRIM37. Thus, TRIM37 ensures accurate chromosome segregation by preventing the formation of centrobin-scaffolded condensates that organize ectopic spindle poles. Mutations in *TRIM37* cause the disorder mulibrey nanism, and patient-derived cells harbor centrobin condensate-organized ectopic poles, leading us to propose that chromosome missegregation is a pathological mechanism in this disorder.

Introduction

TRIM37 is a tripartite motif (TRIM) ubiquitin ligase with an N-terminal RING, B-box, coiled-coil ubiquitin ligase domain (Brigant et al., 2018). Unique among TRIM family ligases, TRIM37 also has a TRAF (tumor necrosis factor receptor–associated factor) domain that mediates protein–protein interactions (Meitinger et al., 2020; Park, 2018). *TRIM37* loss-of-function mutations cause a rare autosomal recessive disorder called mulibrey (for muscle-liver-brain-eye) nanism (Avela et al., 2000; Brigant et al., 2018). Symptoms of mulibrey nanism include pre- and postnatal growth failure, liver enlargement, deregulation of glucose and lipid metabolism (including type 2 diabetes, fatty liver, and hypertension), infertility, and, in ∼20% of cases, overgrowth of the fibrous sac that surrounds the heart (constrictive pericarditis). Mulibrey nanism patients are also plagued with numerous tumors (Karlberg et al., 2009a; Karlberg et al., 2009b; Sivunen et al., 2017). How TRIM37 loss causes the spectrum of symptoms observed in mulibrey nanism patients or renders them cancer prone is not understood.

At the cellular level, TRIM37 has been localized to peroxisomes (Kallijärvi et al., 2002; Wang et al., 2017) and centrosomes (Meitinger et al., 2020). At peroxisomes, TRIM37 was shown to monoubiquitinate the peroxisomal import receptor Pex5, which lent support to the classification of mulibrey nanism as a peroxisomal disorder (Kallijärvi et al., 2002; Wang et al., 2017). A TRIM37 knockout mouse model recapitulated a number of the phenotypes seen in mulibrey nanism patients (Kettunen et al., 2016). *Trim37*$^{-/-}$ mice had growth defects, were infertile, and exhibited elevated fasting blood glucose and low fasting serum insulin levels. After 18 mo, they also exhibited cardiomyopathy, hepatomegaly, fatty liver, and various tumors. However, peroxisome number and morphology were normal in *Trim37*$^{-/-}$ mice, even following a challenge that drives peroxisome biogenesis (Kettunen et al., 2016). Thus, cellular-level defects other than in peroxisomes likely underlie mulibrey nanism pathology.

TRIM37 also localizes to centrosomes (Meitinger et al., 2020), and centrosome-associated proteins feature prominently among TRIM37 interaction partners identified by proximity interaction proteomic analysis (Firat-Karalar et al., 2014; Yeow et al., 2020). Centrosomes, which are organized by small cylindrical organelles called centrioles, are the primary microtubule organizing centers (MTOCs) in animal cells (Banterle and Gönczy, 2017;

[1]Ludwig Institute for Cancer Research, La Jolla, CA; [2]Section of Cell and Developmental Biology, Division of Biological Sciences, University of California, San Diego, La Jolla, CA; [3]Department of Cellular and Molecular Medicine, University of California, San Diego, La Jolla, CA; [4]Laboratory of Protein Dynamics and Signaling, National Institutes of Health, National Cancer Institute, Center for Cancer Research, Frederick, MD.

*F. Meitinger, D. Kong, and M. Ohta contributed equally to this paper; **A. Desai, K. Oegema, and J. Loncarek contributed equally to this paper; Correspondence to Karen Oegema: koegema@health.ucsd.edu; Jadranka Loncarek: jadranka.loncarek@nih.gov.

Breslow and Holland, 2019; Loncarek and Bettencourt-Dias, 2018). Centrioles recruit a proteinaceous matrix called the pericentriolar material (PCM) that nucleates microtubules to catalyze assembly of the mitotic spindle (Mennella et al., 2014; Woodruff et al., 2014). To ensure that mitotic cells have precisely two centrosomes to organize the two poles of a bipolar mitotic spindle, centriole duplication is tightly regulated. In S phase, each mother centriole gives rise to a single daughter centriole in a process controlled by the kinase PLK4 (Banterle and Gönczy, 2017; Breslow and Holland, 2019; Loncarek and Bettencourt-Dias, 2018). TRIM37 was identified in an RNAi screen in HeLa cells for proteins whose knockdown led to an increase in the number of foci containing the centriolar protein centrin (Balestra et al., 2013). This phenotype has been interpreted as TRIM37 loss leading to the formation of extra centrioles by promoting centriole reduplication, in which a single mother centriole gives rise to more than one daughter centriole within a single cell cycle (Balestra et al., 2013). *TRIM37Δ* cells and cells expressing ligase-defective TRIM37 have also been shown to possess an ectopic PLK4-containing condensate (Meitinger et al., 2020). TRIM37 interacts with and ubiquitinates PLK4 but does not alter PLK4 levels, suggesting that rather than promoting its degradation, TRIM37-mediated ubiquitination prevents the incorporation of PLK4 into ectopic assemblies (Meitinger et al., 2020). In live-cell imaging, transiently multipolar spindles were observed in ∼20% of *TRIM37Δ* cells (Meitinger et al., 2016). Whether this low-penetrance spindle phenotype arises from extra centrioles or is due to microtubule organization by ectopic assemblies, such as the PLK4-containing condensate, has not been clarified.

Here, we analyze the impact of TRIM37 loss to define mitotic defects that may contribute to mulibrey nanism. We show that TRIM37 activity does not regulate centriole structure or duplication, or the ability of centrioles to template cilia formation, but instead restrains the formation of ectopic centrosomal protein assemblies that coexist with centrosomes. Cells lacking TRIM37 form a large highly ordered condensate, scaffolded by the centrosomal protein centrobin and containing PLK4, that arises by budding off of the centrosome. In ∼25% of cells, the condensate recruits other centrosomal proteins and acquires MTOC activity during mitotic entry, generating an ectopic spindle pole that elevates chromosome missegregation rates. The aberrant mitotic phenotypes of *TRIM37Δ* cells are suppressed by removing centrobin, which interacts with and is ubiquitinated by TRIM37. We propose that chromosome missegregation resulting from transient multipolarity and multipolar segregation caused by the presence of an ectopic noncentrosomal spindle pole is a major cellular-level pathology contributing to mulibrey nanism that explains why patients with this disorder are cancer prone.

Results

TRIM37 does not control centriole duplication, structure, or the ability of centrioles to form cilia

To determine if TRIM37 loss affects centriole structure or duplication, we used expansion microscopy to analyze centrioles in WT and *TRIM37Δ* RPE1 cells. To assess whether selectively mutating TRIM37 ligase activity was similar to *TRIM37* deletion, we also analyzed *TRIM37Δ* cells stably expressing transgene-encoded WT or ligase mutant TRIM37 (Lig^{mut}; catalytic Cys18 mutated to Arg; Fig. 1 A; Meitinger et al., 2020). After expansion, centrioles were visualized by immunostaining for acetylated tubulin, a marker for centriolar microtubules, and CEP290, a marker for the distal region of centrioles (Kong et al., 2020). Centrioles in *TRIM37Δ* cells appeared structurally normal (Fig. 1 B) and there was no significant difference in the distribution of mother centriole lengths between parental RPE1, *TRIM37Δ*, and *TRIM37Δ* reconstituted with WT or Lig^{mut} TRIM37 (Fig. 1, B and C).

To assess effects on centriole number, we analyzed large populations of cells for each condition. *TRIM37Δ* cells had predominantly two centrioles (single or duplicated) with a small fraction (∼5%) having more than two separated centrioles (Fig. 1, B and D). An even smaller fraction (∼1%) had partial structures labeled with acetylated tubulin that were not full centrioles (Fig. 1, B and D). The minor elevation in cells with increased centriole number was suppressed by expression of WT, but not Lig^{mut}, TRIM37 (Fig. 1 D). Expansion microscopy makes it straightforward to assess centriole overduplication by counting the number of procentrioles per mother centriole in S phase cells. Based on two independent experiments scoring >1,000 S phase cells with duplicating mother centrioles, no centriole overduplication was observed in *TRIM37Δ* or in *TRIM37Δ* cells expressing Lig^{mut} TRIM37. Thus, the ∼5% of cells with extra centrioles observed in *TRIM37Δ* cells do not arise from overduplication in S phase. *TRIM37Δ* RPE1 cells also retained the ability to assemble primary cilia following serum starvation (Fig. 1 E). Ciliation frequency and ciliary length were slightly elevated in the *TRIM37Δ* cell line relative to parental RPE1 cells (Fig. 1 E and Fig. S1 A); however, whether this results from TRIM37 loss or reflects clonal variation is unclear.

Collectively, these results indicate that TRIM37 is not regulating centriole duplication, structure, or the ability to assemble cilia. The minor proportion of cells with elevated centriole number observed in *TRIM37Δ* cells likely arise indirectly as a consequence of mitotic defects, as described below.

Loss of TRIM37 leads to the formation of a condensate containing centrobin and PLK4

In a localization screen of centrosomal components comparing *TRIM37Δ* RPE1 cells to control *USP28Δ* RPE1 cells, we found that centrobin (encoded by *CNTROB*) localized prominently to a noncentrosomal focus in *TRIM37Δ* cells; no such focus was observed in control *USP28Δ* cells (Fig. 1 F). Centrobin localizes to procentrioles and to daughter centrioles that have not yet duplicated (Zou et al., 2005) and has been implicated in ciliogenesis (Ogungbenro et al., 2018; Reina et al., 2018). In our experiments, we used *USP28Δ* RPE1 cells generated in parallel to the *TRIM37Δ* RPE1 cells as a control, because loss of *USP28* inactivates a sensor pathway that triggers p53 activation in response to extended mitotic duration, which facilitates analysis of phenotypes in the presence and absence of centrosomes (Meitinger et al., 2016).

The noncentrosomal structure observed with centrobin staining also labeled for PLK4, indicating that it is the same

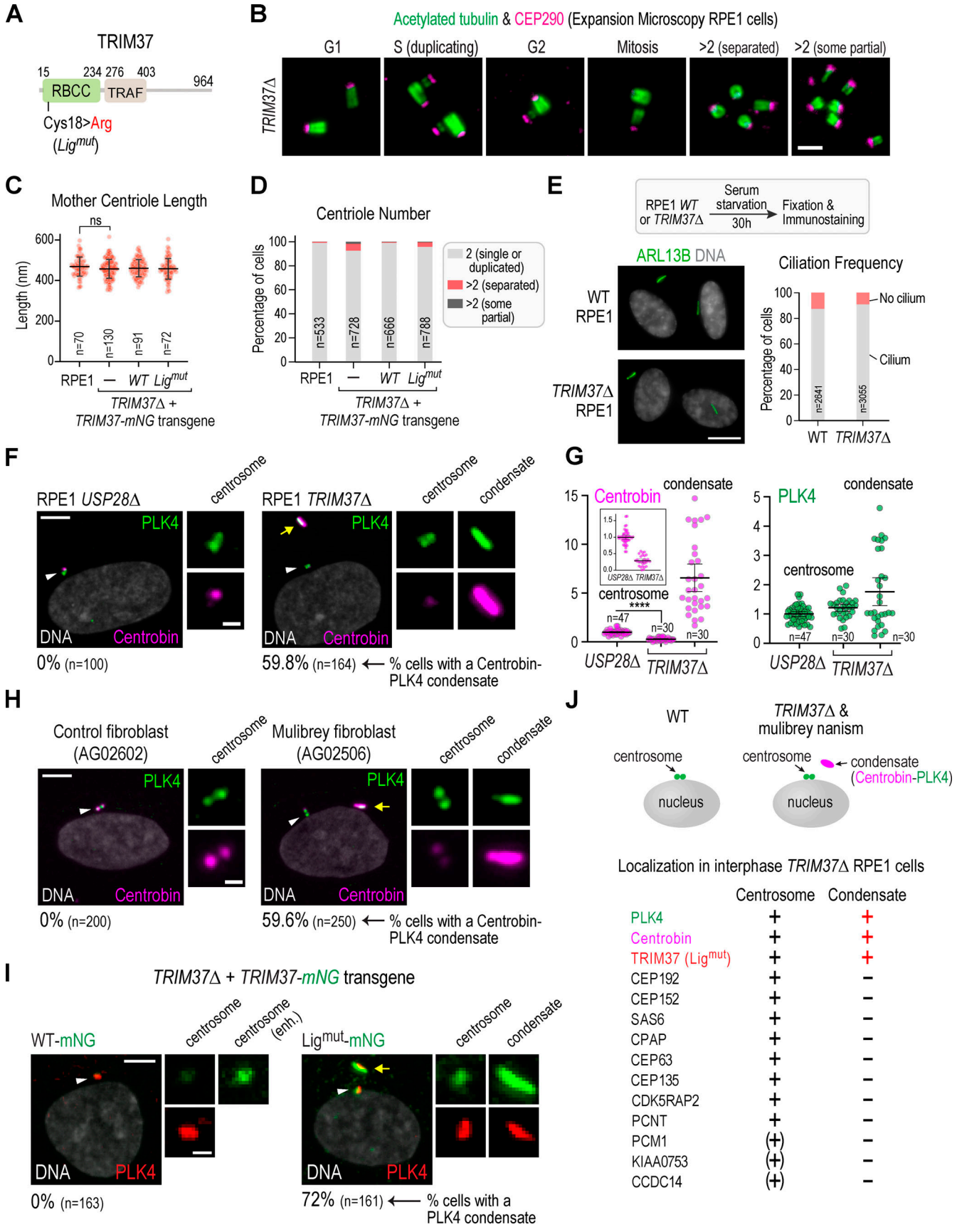

Figure 1. **Consequences of TRIM37 loss in interphase RPE1 cells and mulibrey nanism patient-derived fibroblasts. (A)** Schematic of TRIM37, which has a RING–B-box–coiled-coil (RBCC) ubiquitin ligase domain. Mutation of catalytic Cys18 to Arg (Lig^{mut} TRIM37) disrupts ligase activity. **(B)** Expansion microscopy

of centrioles colabeled for acetylated tubulin and the distal centriole component CEP290. Normal centrioles at different cell cycle stages and rare aberrant centriolar configurations are shown in *TRIM37Δ* RPE1 cells. Scale bar, 2 µm. **(C)** Quantification of mother centriole length from expansion microscopy of the indicated conditions. Error bars represent standard deviation. n, number of centrioles; ns, not significant, based on a *t* test. **(D)** Quantification of centriole number for the indicated cell lines following expansion microscopy as in B. Normal G1, S, G2, and M centriolar configurations were counted as "2 (single or duplicated)". For B–D, cells were expanded twice with similar results; images and quantification of centriole length are from one experiment, and the centriole number data is pooled from both experiments. **(E)** Analysis of ciliogenesis, assessed by ARL13B labeling, in control RPE1 and *TRIM37Δ* RPE1 cells. Scale bar, 10 µm. The experiment was performed twice, once in triplicate and once in duplicate, with similar results; ciliation frequency from one experiment is shown here and from the second experiment in Fig. S1 A. **(F)** Immunostaining of *TRIM37Δ* and control *USP28Δ* RPE1 cells for centrobin and PLK4. Scale bars, 5 µm and 1 µm (insets). **(G)** Quantification of immunofluorescence signals at centrosomes in control *USP28Δ* cells and at centrosomes and condensates in *TRIM37Δ* cells. The signal for both centrosomes in a cell was measured together. Values were normalized relative to the mean centrosomal signal in *USP28Δ* cells; inset in the centrobin graph shows centrosome signals plotted on a different *y*-axis scale. Mean and 95% confidence interval (CI) are plotted on top of individual values; P value is from an unpaired *t* test. The condensate signal values plotted here are the same as those shown in Fig. S4 B (–Dox). Experiments in F and G were repeated twice; images and quantification are from one experiment. **(H)** Immunostaining of control and mulibrey nanism patient-derived fibroblasts. Scale bars, 5 µm and 1 µm (insets). The experiment was performed once; data for each cell line were pooled from three replicate wells imaged in parallel. **(I)** Localization of mNG-fused TRIM7 (WT or Lig^{mut}) expressed in *TRIM37Δ* cells. TRIM37 activity reduces its own levels; hence, the signal for WT TRIM37-mNG was enhanced to show centrosomal localization. Scale bars, 5 and 1 µm (insets). The experiment was performed once; an equivalent experiment with similar results was performed using an HA tag shown in (Meitinger et al., 2020). **(J)** Top: Schematic of condensate observed in *TRIM37Δ* RPE1 cells and mulibrey nanism patient fibroblasts. Bottom: Summary of the localization of centrosomal components in *TRIM37Δ* cells; components shown in brackets localize to centriolar satellites. Analysis of CPAP, CEP63, CEP135, PCM1, KIAA0753, and CCDC14 is from Meitinger et al. (2020) and was conducted with PLK4 colabeling. In F, H, and I, centrosomes (white arrowheads) and the condensate (yellow arrows) are indicated, and numbers below images indicate percentage of cells with a condensate.

condensate previously described based on PLK4 staining in *TRIM37Δ* cells (Meitinger et al., 2016; Meitinger et al., 2020). Approximately 60% of interphase *TRIM37Δ* cells had a condensate that was spatially distinct from the centrosome, and all condensates colabeled for centrobin and PLK4. Quantification of signal intensities indicated that condensates varied in size and that centrosomal centrobin levels were significantly reduced in *TRIM37Δ* cells with a condensate, whereas centrosomal PLK4 levels were not (Fig. 1 G). Similar condensates were observed in a fibroblast cell line from a mulibrey nanism patient (Fig. 1 H), consistent with biallelic loss of *TRIM37* in this disorder.

Costaining with centrobin and the centriolar/centrosomal proteins SAS6, CEP152, CEP192, CDK5RAP2, and PCNT indicated that these components were not present in the condensate (Fig. S1 B), consistent with prior colabeling conducted with PLK4 (Meitinger et al., 2020). Catalytic mutants of ubiquitin ligases can act as substrate traps; consistent with this, an mNeonGreen (mNG) fusion with Lig^{mut} TRIM37 concentrated prominently at the condensate, in addition to localizing to centrosomes (Fig. 1 I). Thus, the condensates in *TRIM37Δ* cells contain centrobin and PLK4 and, when expressed, Lig^{mut} TRIM37, but not other centrosomal components (Fig. 1 J; Meitinger et al., 2020).

Condensates exhibit two related highly ordered morphologies

To analyze the structure of the condensates resulting from *TRIM37* deletion, we employed correlative light and electron microscopy (CLEM) and super-resolution microscopy. For CLEM, we used the *TRIM37Δ* RPE1 cell line stably expressing Lig^{mut} TRIM37-mNG, which allows condensate identification by fluorescence microscopy (Fig. 2 A). CLEM of the condensates revealed a highly ordered striated morphology, with electron-dense stripes spaced ∼90 nm apart (Fig. 2 A); in the same cells, centrosomes with localized Lig^{mut} TRIM37-mNG and a normal pair of centrioles were present (Fig. 2 A; cell 1, centrosome, sections 1–4). Similar structures were observed in 9 out of 12 cells analyzed by CLEM. Serial sectioning of large condensates suggests formation by coalescence of smaller width structures (e.g., condensate in cell 1 in Fig. 2 A). In one cell processed for CLEM, we observed condensates that in addition to striated densities also contained regions with punctate electron densities arranged in hexagonally packed sheet-like configuration (Fig. 2 B and Fig. S1 C). In serial sections, the hexagonally packed punctate morphology transitioned to a striped morphology associated with narrowing of the width of the structure (e.g., sections 2 and 3 of condensate in Fig. 2 B).

To confirm the strikingly regular morphology of the condensates observed by CLEM, we employed three superresolution imaging approaches: expansion structured illumination microscopy (Exp-SIM), stochastic optical reconstruction microscopy (STORM), and stimulated emission depletion (STED) microscopy (Fig. 3, A–D; and Fig. S1 D). Centrobin was detected using an antibody raised against the whole protein, and PLK4 was detected using an antibody against the C-terminal 157 amino acids. Only the centrobin antibody worked for Exp-SIM, but both antibodies worked for STED and STORM. As these methods do not require a reference fluorescence signal, we analyzed *TRIM37Δ* cells and *TRIM37Δ* cells expressing Lig^{mut} TRIM37-mNG. All three methods revealed condensate morphologies that fell into the classes observed by CLEM: (1) "linear striated" structures, (2) hexagonally packed "punctate sheets", and (3) "hybrid" structures with regions exhibiting both morphologies (Fig. 3, A–D). In *TRIM37Δ* cells expressing Lig^{mut} TRIM37-mNG, where a direct comparison can be made between the CLEM and super-resolution analysis, predominantly linear striated structures were observed with interstripe distances nearly identical to those measured by CLEM (Fig. 3, C and D). All three condensate morphologies were observed in both cell lines, but *TRIM37Δ* cells had a higher percentage with punctate sheet-like morphology while linear striated condensates predominated in the *TRIM37Δ* cells expressing Lig^{mut} TRIM37-mNG (Fig. 3 C). Quantification of the interstripe and interpuncta dimensions revealed consistent values independently of the method employed and suggested that the interstripe distance in the linear structures was modestly larger than the interpuncta distance in the sheet-like structures (Fig. 3 D).

We conclude that loss of TRIM37 or its ligase activity leads to the formation of condensates that exhibit two related highly

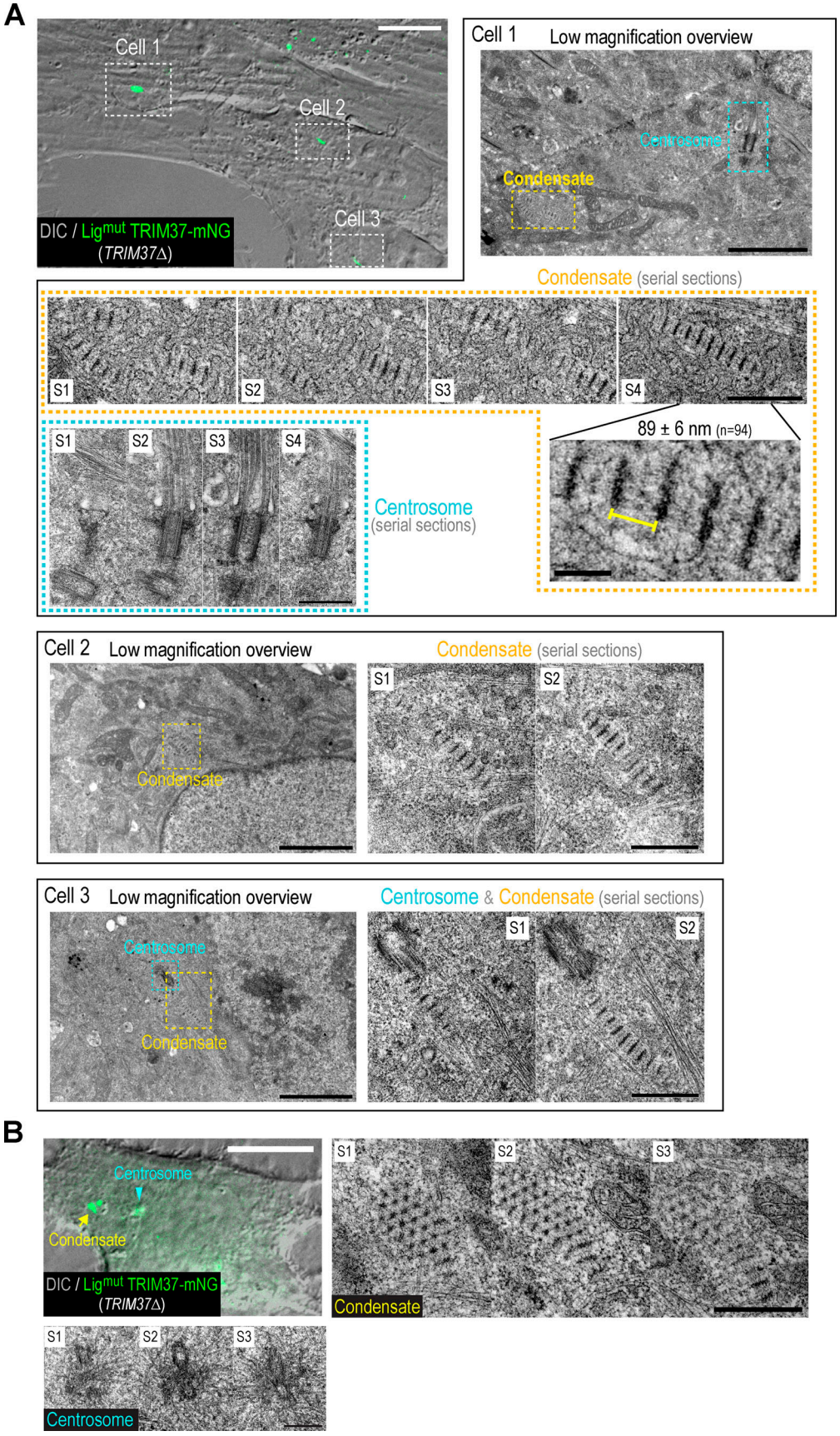

Figure 2. **CLEM of *TRIM37Δ* cells expressing mNG-fused Lig^{mut} TRIM37. (A)** Top left: Overlay of DIC and mNG fluorescence channels for three cells analyzed by serial section EM. Colored boxes in low-magnification (1,900×) views indicate the mNG-labeled condensate and the centrosome.

Higher-magnification views (11,000×) of serial sections through the condensates reveal a highly ordered striated structure; a zoomed-in view shows regularly spaced stripes ∼90 nm apart; n, number of measurements. In cell 3, the condensate is associated with a centrosome. **(B)** Left: DIC-mNG overlay of a cell with a condensate close to a centrosome; this cell is in early mitosis. High-magnification view (11,000×) reveals a sheet-like object composed of hexagonally packed electron-dense puncta; the bottom part of the condensate appears to narrow and transition to the striated pattern seen in A. White scale bars in DIC-mNG overlay images, 20 µm. Black scale bars in EM images: low magnification, 2 µm; condensate and centrosome serial sections, 0.5 µm; zoomed-in view, 0.1 µm. S, section.

ordered morphologies. The existence of hybrid condensates suggests that there may be interconversion between these two morphologies. Linear striated structures are enriched following expression of Lig^{mut} TRIM37-mNG in *TRIM37Δ* cells, suggesting that binding of the catalytically inactive ligase may preferentially stabilize this morphology.

Condensates form by budding off of centrosomes

We next sought to understand how condensates form in the absence of TRIM37 and why there is typically one such condensate per cell. Structured illumination microscopy (SIM), in conjunction with markers for specific centriolar domains, indicated that TRIM37 is broadly localized throughout the centrosome, suggesting that it acts locally at the centrosome to prevent condensate formation (Fig. S1 E). To image condensate formation in living cells, we employed a *TRIM37Δ* cell line expressing Lig^{mut} TRIM37-mNG. As cells typically have one condensate, following mitosis, one daughter cell inherits the condensate and the other is born without a condensate (Fig. 3 E). In cells born without a condensate, Lig^{mut} TRIM37-mNG hyperaccumulated around the centrosome, and, after some time, a portion of the accumulated material budded off to form a condensate (Fig. 3 E and Video 1). In the daughter cell that inherited a condensate after division, no hyperaccumulation of the probe or new condensate formation occurred (Fig. 3 E and Video 1). Condensates budded off of the centrosome at varying times, suggesting that budding is not cell cycle regulated (Fig. 3 F). In addition, condensate formation and budding occurred with similar frequency following acute inhibition of PLK4 by centrinone (Fig. 3 F), indicating that PLK4 kinase activity is not required. In rare cases, we observed two condensates that fused into one (Fig. S1 F); the fused condensate was elongated and did not adopt a spherical shape characteristic of liquid-like condensates. We conclude that condensate assembly occurs at centrosomes and that this assembly is normally prevented by the ubiquitin ligase activity of TRIM37.

Condensates exhibit ectopic spindle pole activity during mitosis

We next focused on the consequences of TRIM37 loss–induced condensate formation on mitosis. Expansion microscopy coupled to labeling for acetylated tubulin revealed that ∼30% of mitotic *TRIM37Δ* cells had chromosome configurations that suggested the presence of an extra spindle pole; of the cells with a multipolar chromosome configuration, the majority (∼75%) had two centrosomes, with the remainder having either an extra centrosome or a small focus of acetylated tubulin at the third pole (Fig. 4 A). This initial analysis suggested that ∼20–25% of *TRIM37Δ* prometaphase/metaphase cells have an ectopic noncentrosomal spindle pole that is likely formed by the condensate. Consistent with the idea that condensates can nucleate microtubules to form an ectopic pole, optical sectioning through immunofluorescence images of prometaphase/metaphase *TRIM37Δ* cells colabeled for centrobin and microtubules revealed that ∼25% of the condensates were at the center of a focused array of microtubules (Fig. 4, B–D). Acquisition of MTOC activity by condensates correlated with transition into prometaphase/metaphase (Fig. 4, B and D) and was associated with recruitment to the condensate of the microtubule nucleation-promoting centrosomal components CEP192, PCNT, CDK5RAP2, and γ-tubulin (Fig. S2 A), none of which are present on condensates in interphase (Fig. S1 B and Fig. 1 J). In microtubule regrowth assays, approximately half of the condensates in prometaphase/metaphase cells exhibited microtubule-nucleating activity (Fig. S2 B).

To address whether the ectopic poles observed in *TRIM37Δ* RPE1 cells are relevant to mulibrey nanism, we analyzed mitotic patient-derived fibroblasts. No condensates were observed in control mitotic primary fibroblasts, whereas 21 of 22 mitotic mulibrey fibroblast cells had a condensate. In 9 of these mitotic cells (∼40%), the condensate organized an ectopic spindle pole (Fig. 4 E). Thus, formation of ectopic spindle poles by condensates is observed in both RPE1 *TRIM37Δ* cells and in mulibrey nanism patient-derived fibroblasts.

To complement the immunofluorescence in fixed cells, we conducted live imaging of microtubules, which revealed ectopic spindle poles during ∼25% of mitoses in *TRIM37Δ* cells (Fig. 4, F and H; and Video 2). The formation of ectopic poles was suppressed by the expression of WT TRIM37-mNG, but not Lig^{mut} TRIM37-mNG (Fig. 4, F–H). Two-color live imaging of microtubules and of Lig^{mut} TRIM37-mNG as a condensate marker revealed three phenotypes (Fig. 4, G and H; and Video 3): (1) condensates that did not nucleate microtubules or generate an ectopic spindle pole (bipolar configuration), (2) condensates that generated an ectopic pole that ultimately clustered with one of the centrosomes to enable bipolar segregation (transient multipolarity), and (3) condensates that generated an ectopic pole that persisted into anaphase (multipolar segregation).

A small number of mitotic *TRIM37Δ* cells (∼5%) harbor an aberrant number of centrioles (Fig. 1, B and D), although no centriole overduplication was observed in >1,000 S phase *TRIM37Δ* cells. To address the origin of these extra centrioles, we analyzed a large number of mitotic *TRIM37Δ* cells labeled for centrobin. In *TRIM37Δ* mitotic cells with two centrosomes and a condensate, ∼27% exhibited a multipolar configuration with the condensate sitting at the third pole; interestingly, in ∼2% of the cells, a bipolar chromosome configuration was observed in which the condensate formed one pole and both centrosomes

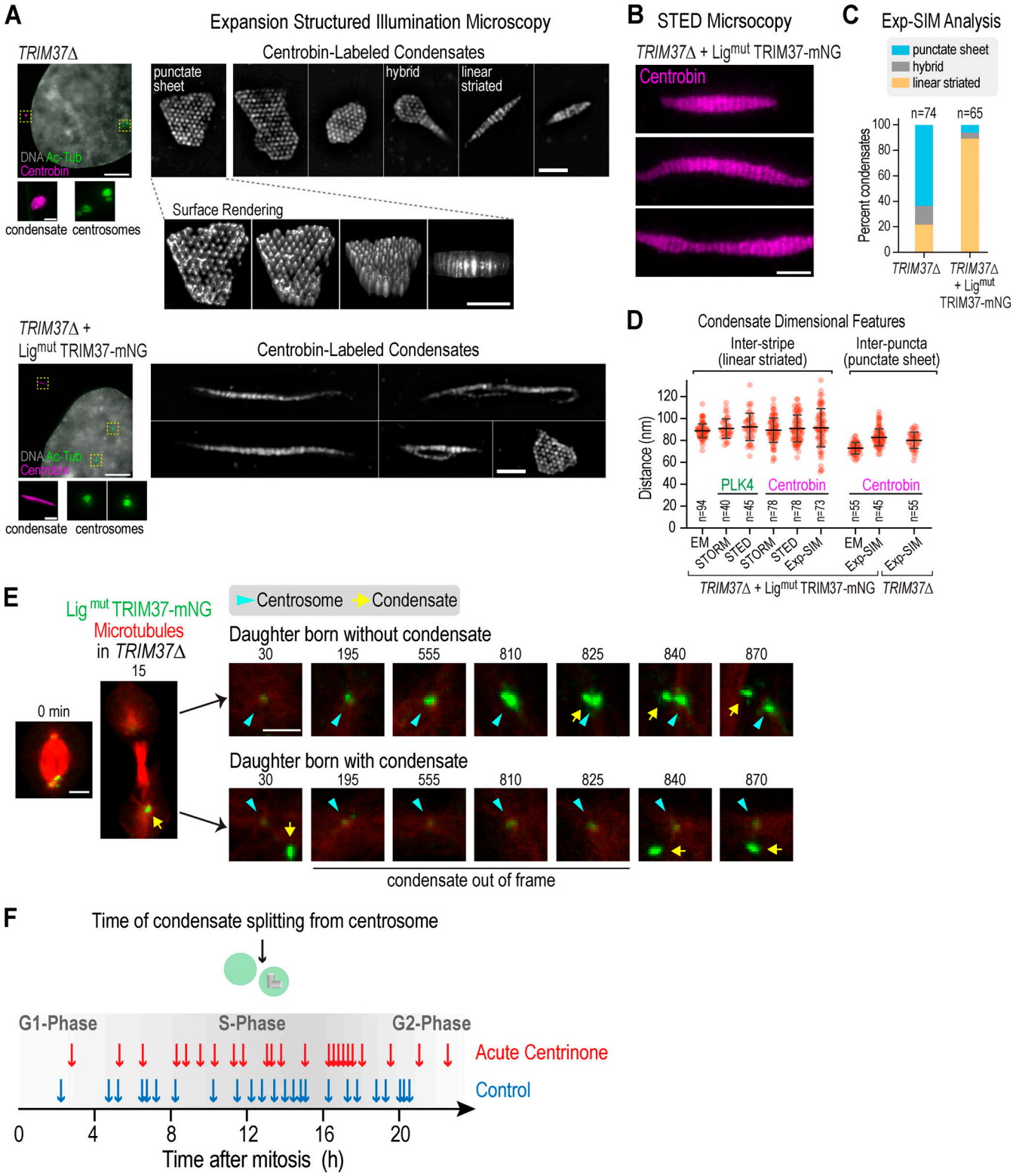

Figure 3. **Condensates exhibit two related types of structural organization and form by budding off of centrosomes. (A)** Exp-SIM of condensates in *TRIM37Δ* cells and in *TRIM37Δ* cells expressing Lig^{mut} TRIM37 immunostained for centrobin. Widefield images are shown on the left; black-and-white images are examples of condensates from different cells. Surface rendering of a condensate in a *TRIM37Δ* cell is also shown. Scale bars: widefield, 20 µm and 2 µm (panels below image); Exp-SIM, 2 µm. **(B)** STED microscopy images showing the linear, striated condensates. Scale bars, 0.5 µm. Experiment performed three times with similar results. **(C)** Quantification of condensate morphologies (see A for example images) from the Exp-SIM analysis. n, number of condensates. The experiment shown in A and C was performed twice with similar results; data shown are from one experiment. **(D)** Quantification of interstripe or interpuncta distance measured using different methods; n, number of measurements. 10th–90th percentile box-and-whiskers plots with outliers are shown. **(E)** Live imaging of Lig^{mut} TRIM37-mNG-labeled condensates in a *TRIM37Δ* cell expressing mRuby-fused MAP4 microtubule-binding domain to label microtubules; the

centrosome (cyan arrowhead) and the condensate (yellow arrow) are indicated. Scale bars, 5 µm. Times are in minutes. **(F)** Summary of timing of condensate splitting from the centrosome in 24 imaged untreated cells (blue arrows) and 23 imaged cells acutely treated with centrinone (red arrows). Time is in hours relative to mitosis of each mother cell. The experiment shown in E and F was performed once; data for each condition was pooled from two replicate wells imaged in parallel.

clustered at the other pole (Fig. 4, I and J). This configuration, which we refer to as "dominant," would lead to generation of one daughter cell with twice the normal number of centrioles and a second daughter cell without centrioles, which would likely activate de novo centriole assembly (which lacks copy number control) in the subsequent S phase. Division of cells with this dominant configuration caused by a condensate-organized spindle pole, along with potential cytokinesis failure of multipolar division configurations, likely accounts for the generation of *TRIM37Δ* cells with aberrant centriole numbers. We speculate that such cells are constantly generated and being selected against, explaining the persistence of a small percentage of cells with aberrant centriole numbers in the clonally derived *TRIM37Δ* cell population.

Condensate-based ectopic spindle poles elevate chromosome missegregation in *TRIM37Δ* cells

We next addressed the functional consequences of ectopic condensate-based spindle poles in *TRIM37Δ* cells. Fixed analysis of chromosome segregation, comparing WT and *TRIM37Δ* RPE1 anaphase-telophase cells with two centrosomes, revealed a significantly elevated rate of multipolar segregation (~6.5% of anaphase/telophase cells) and of lagging chromosomes (~3% of anaphase/telophase cells; Fig. 5 A). Consistent with this observation, the frequency of cells harboring micronuclei was also significantly elevated in the *TRIM37Δ* cell population relative to parental RPE1 cells (Fig. 5 B).

To independently assess chromosome missegregation rates in *TRIM37Δ* cells, we performed FISH analysis of two chromosomes (17 and 18) in telophase cells. We found a significant number of missegregation events for these chromosomes in both bipolar and multipolar configurations (Fig. 5 C), as well as properly segregating but aneuploid cells (Fig. 5 C, bipolar aneuploid), indicative of a missegregation event in a prior division. Collectively, this analysis indicates that the ectopic spindle poles formed by condensates in *TRIM37Δ* cause significant chromosome missegregation, generating aneuploid progeny.

Centrobin is required to form condensates in the absence of TRIM37

To causally link condensates to the observed mitotic defects in *TRIM37Δ* cells, we assessed the molecular requirements for condensate formation using inducible CRISPR/Cas9-based knockouts of *CNTROB* and *PLK4*. Inducible knockouts were generated in *TRIM37Δ* RPE1 cells and *USP28Δ* RPE1 cells, which served as controls. The strategy used to target *CNTROB* is shown in Fig. S3 A, and efficient generation of mutations in *CNTROB* after Cas9 induction in both the *TRIM37Δ* and *USP28Δ* cell lines was confirmed by sequencing (Fig. S3 A). The inducible *PLK4* knockout was previously generated and shown to result in efficient generation of mutations and centrosome loss after 4-d induction (Meitinger et al., 2020).

Inducible *CNTROB* knockout caused loss of centrosomal centrobin signal in *USP28Δ* RPE1 cells, confirming efficacy of the knockout (Fig. 6 A and Fig. S3 B); no defect in centrosome number or proliferation was observed in the 4-d period after induction (not shown). In *TRIM37Δ* RPE1 cells, inducible *CNTROB* knockout led to loss of condensates labeled with centrobin and PLK4; by contrast, PLK4 signal was still detected at centrosomes (Fig. 6 A). Conducting the same analysis following inducible *PLK4* knockout showed that 4-d induction of the *PLK4*-targeting gRNA resulted in formation of acentrosomal cells. Approximately 12% of these acentrosomal cells lacked a centrobin and PLK4-containing condensate; the remaining cells retained a condensate that labeled for both centrobin and PLK4, although condensates in *TRIM37Δ iPLK4 KO* cells varied in size and on average had less of both markers than condensates in *TRIM37Δ* cells (Fig. S4, A and B). These results suggest that PLK4 does not turn over after it is incorporated into the condensates. A caveat with interpreting this result is that centriole loss due to PLK4 protein depletion in *TRIM37Δ* cells delays mitosis and triggers p53-dependent arrest (Meitinger et al., 2020). This cessation of proliferation following inducible *PLK4* knockout, which is not observed after removal of centrobin, confounds analysis of the role of PLK4 in condensate formation.

We conclude that centrobin is essential to build the structured condensates in *TRIM37Δ* cells. We thus refer to these structures as centrobin-scaffolded condensates.

Ectopic centrin foci in *TRIM37Δ* cells are independent of the centrobin-scaffolded condensate

TRIM37 depletion by RNAi in HeLa cells has been reported to result in supernumerary foci containing the centriolar marker centrin (Balestra et al., 2013). We confirmed that centrin, in addition to localizing to the centrosome, is present in ectopic foci in ~60% of interphase *TRIM37Δ* RPE1 cells. The number of centrin foci per cell was variable, typically between one and five, and centrin foci were smaller than the condensate (Fig. 6 B). One centrin focus partially colocalized with the condensate (see magnified view of the condensates in Fig. 6 B and Fig. S4 C; 96% of the condensates had a colocalized centrin focus, $n = 100$). Additional centrin foci that did not colocalize with the condensate were often also present in *TRIM37Δ* cells (Fig. 6 B and Fig. S4 C).

Removal of centrobin using the inducible *CNTROB* knockout eliminated the condensate but did not eliminate centrin foci (Fig. 6 B); the frequency of cells with centrin foci and the number of centrin foci per cell were mildly elevated in *TRIM37Δ* cells lacking centrobin (Fig. 6 B). No PLK4 was detected in the centrin foci observed in *CNTROB* knockout cells (Fig. 6 B). We conclude that centrin foci in *TRIM37Δ* cells do not require the centrobin-scaffolded condensate to form. Thus, TRIM37 independently suppresses formation of a centrobin-scaffolded condensate and of centrin foci (Fig. 6 C).

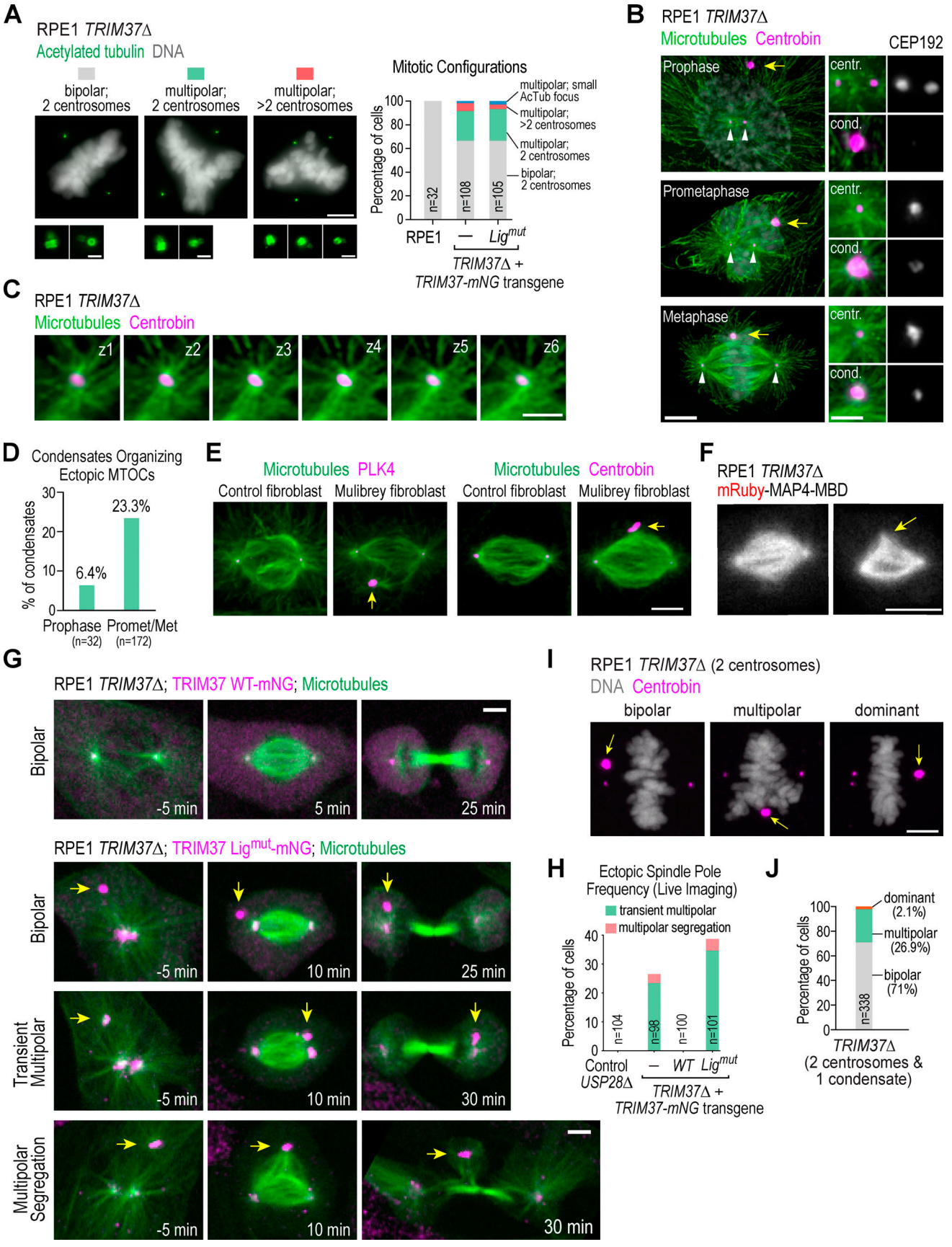

Figure 4. **Condensates form ectopic spindle poles during mitosis in *TRIM37Δ* RPE1 and mulibrey nanism patient cells. (A)** Left: Expansion microscopy images of mitotic *TRIM37Δ* RPE1 cells labeled for acetylated tubulin showing three mitotic configurations. Right: Quantification of mitotic configurations in the

indicated cell lines; note that the rarest category, multipolar with a small acetylated tubulin focus, is marked in blue. Scale bars, 20 µm and 2 µm (insets). The experiment was performed three times; quantification was of the pooled data. **(B)** Images of mitotic cells at different stages stained for microtubules, centrobin, and CEP192; centrosomes (white arrowheads) and condensates (yellow arrows) are marked. Scale bars, 5 µm and 2 µm (insets). **(C)** Z sections spaced 0.2 µm apart through a metaphase condensate. Scale bar, 2 µm. The experiment in B and C was performed three times. **(D)** Quantification of condensate-associated ectopic MTOCs in mitotic *TRIM37Δ* cells. n, number of condensates. **(E)** Control and mulibrey nanism primary fibroblasts labeled for microtubules and PLK4 (left) or centrobin (right). The condensate (arrows) is marked. Scale bar, 5 µm. Each experiment was performed once. **(F)** Stills from live imaging analysis of microtubules labeled by expression of mRuby-MAP4-MBD in *TRIM37Δ* RPE1 cells. Images are of spindles in two different cells. Arrow points to an ectopic spindle pole. Scale bar, 10 µm. The experiment was performed once. **(G)** Stills from live imaging of *TRIM37Δ* cells expressing mRuby-MAP4-MBD (pseudocolored green) and WT TRIM37-mNG or Lig^{mut} TRIM37-mNG (pseudocolored magenta). Three observed phenotypes of mitotic *TRIM37Δ* cells with a Lig^{mut} TRIM37-mNG-labeled condensate (arrows) are shown. Times are in minutes; 0 min is the first time point after nuclear envelope breakdown. Scale bars, 5 µm. **(H)** Frequency of ectopic spindle poles observed in the indicated conditions analyzed by live imaging of microtubules; cells that exhibited eventual multipolar segregation are indicated. n, number of imaged cells. For G and H, the data from three independent experiments were pooled. **(I)** Immunostaining of the three configurations observed for mitotic cells with a condensate (arrows) and the normal number of two centrosomes. Scale bar, 5 µm. **(J)** Relative frequency of the three configurations shown in I. For I and J, the experiment was performed once; data were pooled from seven replicate wells imaged in parallel.

Removal of the condensate by inducible knockout of *CNTROB* suppresses ectopic spindle pole formation in *TRIM37Δ* cells

In a significant proportion (~20–30%) of mitotic *TRIM37Δ* cells, an ectopic noncentrosomal spindle pole is observed with a condensate at its center. To causally link the condensate to the formation of ectopic poles, we employed the inducible *CNTROB* knockout followed by fixed analysis and live imaging. Inducing *CNTROB* knockout in *TRIM37Δ* cells for 4 d suppressed the formation of ectopic spindle poles in fixed prometaphase and metaphase cells (Fig. 7, A and B). Centrin foci were still observed in these cells lacking centrobin (Fig. S4 C). Live imaging of chromosome dynamics revealed that centrobin removal suppressed both transient multipolarity, which is evident in the chromosome configuration, and the multipolar segregation observed in *TRIM37Δ* cells (Fig. 7, C and D; and Video 4). *CNTROB* knockout also suppressed the mild but statistically significant increase in mitotic duration observed in *TRIM37Δ* cells (Fig. 7 D). Thus, condensates built on a centrobin scaffold are responsible for the formation of ectopic spindle poles that perturb spindle assembly and chromosome segregation in the absence of TRIM37.

Centrobin interacts with TRIM37 and is ubiquitinated in a TRIM37-dependent manner

Centrobin is essential for formation of condensates in *TRIM37Δ* cells, suggesting that centrobin may be a direct target of TRIM37's ubiquitin ligase activity. Consistent with this idea, centrobin protein level was elevated ~3.5-fold in *TRIM37Δ* cells (Fig. 8 A); by contrast, RNA-Seq indicated that *CNTROB* mRNA levels were unchanged (Meitinger et al., 2020). To determine if TRIM37 binds to and regulates centrobin stability, we used a human cell expression system to coexpress centrobin with WT or Lig^{mut} TRIM37. We analyzed crude extracts to assess the effect of TRIM37 ligase activity on total centrobin levels and assayed the formation of insoluble centrobin condensates by centrifugation to generate supernatant and pellet fractions; in addition, we analyzed interaction between centrobin and TRIM37 in the supernatant (Fig. 8 B). Comparison of centrobin levels in crude extracts indicated that coexpression with WT TRIM37 reduced the total amount of centrobin protein approximately threefold compared with expression of centrobin alone (Fig. 8, C and E; and Fig. S5 A). TRIM37's ligase activity was required for the reduction in centrobin levels (Fig. 8, C and E; and Fig. S5 A). When expressed on its own, the majority of centrobin was present in the pellet (Fig. 8, D and E; and Fig. S5 B). While quantitative recovery of centrobin from the pellet was challenging even under denaturing conditions, leading to variability in measured values, coexpression of WT TRIM37 consistently increased the relative solubility of centrobin, measured as a decrease in the ratio between the amount in the pellet and supernatant (pellet/supernatant ratio; Fig. 8, D and E; and Fig. S5 B); by contrast, coexpression of Lig^{mut} TRIM37 did not (Fig. 8, D and E; and Fig. S5 B).

The above analysis additionally revealed that Lig^{mut} TRIM37, which is soluble when expressed on its own, sedimented into the insoluble pellet fraction when coexpressed with centrobin (Fig. 8, D and E). As ligase-inactive forms of ubiquitin ligases can act as substrate traps, this result is consistent with centrobin being a substrate of TRIM37. In support of this idea, Lig^{mut} TRIM37 coimmunoprecipitated with the centrobin that remained in the supernatant (Fig. 8 F and Fig. S5 C). WT TRIM37 is expressed at a much lower level than Lig^{mut} TRIM37 because TRIM37 ligase activity reduces its own stability, a common property of RING family ubiquitin ligases (de Bie and Ciechanover, 2011). Consistent with an interaction between the two proteins, WT TRIM37 could also be coimmunoprecipitated with centrobin when it was partially stabilized by treating the cells with the proteasome inhibitor MG132 (Fig. S5 D). Introduction of epitope-tagged ubiquitin into the coexpression revealed that immunopurified centrobin was ubiquitinated when coexpressed with WT, but not Lig^{mut}, TRIM37 (Fig. 8 G). TRIM37-dependent ubiquitination of centrobin was associated with a decrease in centrobin levels (Fig. 8 G).

The ability of centrobin to greatly decrease the solubility of Lig^{mut} TRIM37 suggests that they are stably associated. To assess if Lig^{mut} TRIM37 is also stably associated with condensates in cells, we conducted photobleaching analysis of Lig^{mut} TRIM37-mNG–labeled condensates in *TRIM37Δ* cells. Lig^{mut} TRIM37 exhibited no detectable turnover on condensates in ~20 min (Fig. 8, H and I; and Video 5), in agreement with the conclusions of the coexpression analysis.

Collectively, these data indicate that TRIM37 directly binds to centrobin and ubiquitinates it to control its levels. TRIM37 may regulate centrobin levels by ubiquitination-dependent

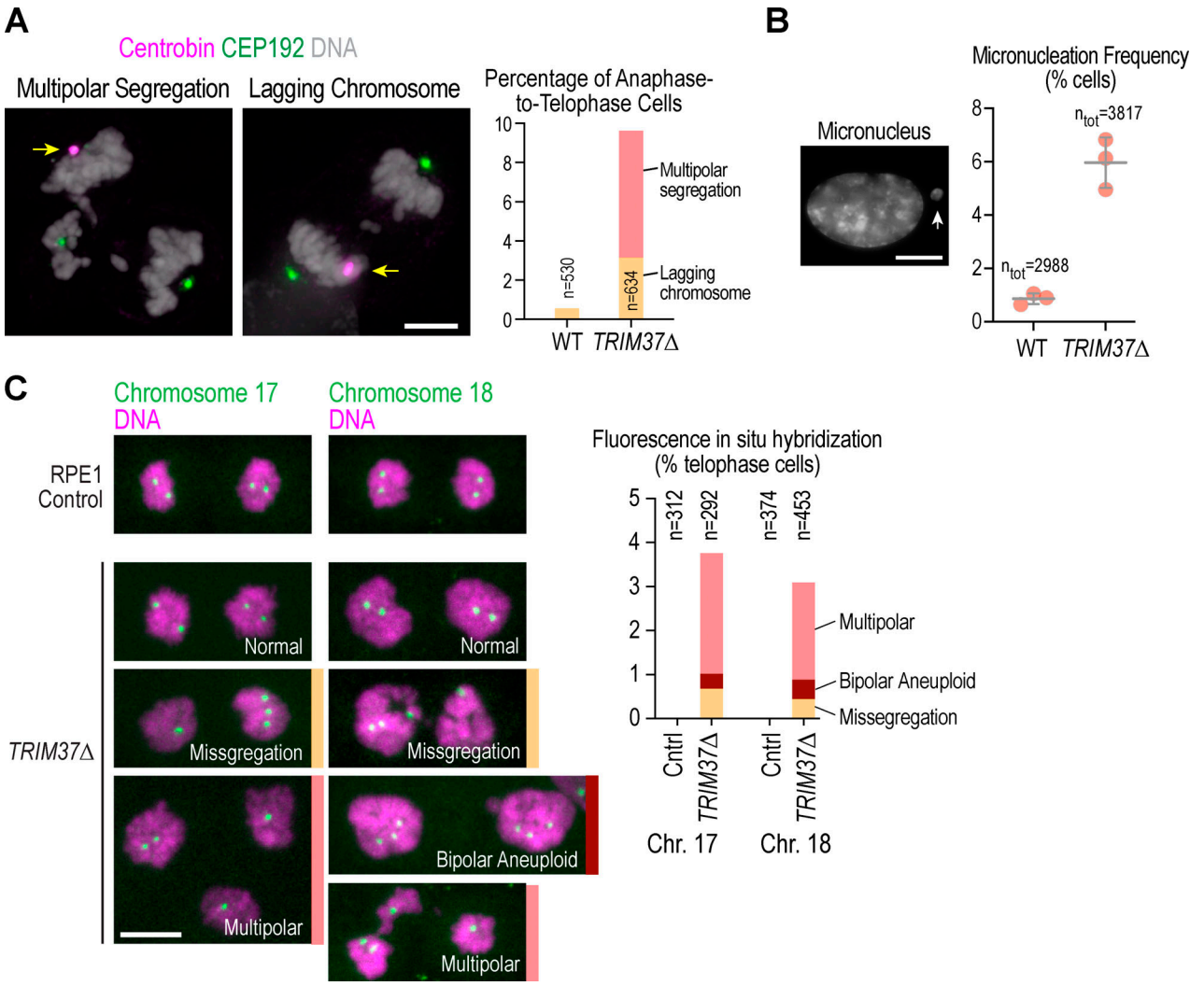

Figure 5. **Condensate-based ectopic spindle poles cause chromosome missegregation. (A)** Fixed analysis of chromosome segregation in anaphase-to-telophase stage cells. Left: Images of multipolar segregation and lagging chromosomes; the condensate (arrows) is marked. Graph on the right plots the frequency of these events in control and *TRIM37Δ* RPE1 cells. Scale bar, 5 µm. Pooled data from six independent samples. **(B)** Analysis of micronuclei frequency. Left: Image of a cell with a micronucleus (arrow). Right: Graph of results from three experiments together with the mean; error bars represent standard deviation, and n_{tot} is the total number of cells scored. Scale bar, 5 µm. **(C)** FISH analysis of chromosomes 17 and 18 in telophase cells. Left: Example images of different classes of telophase figures observed. Right: Quantification of the different categories. The experiment was performed once. Scale bar, 10 µm.

degradation, or it may modify centrobin with ubiquitin to prevent self-association, with the increase in centrobin levels in the absence of TRIM37 being an indirect consequence of the formation of stable insoluble condensates. Distinguishing these possibilities will require future biochemical and structural analysis.

Centrobin is dispensable for the formation of PLK4-scaffolded foci that accelerate acentrosomal spindle assembly in *TRIM37Δ* cells

Much of the prior functional analysis of TRIM37 in dividing cells has focused on cells that lack centrosomes due to inhibition of PLK4 kinase activity (Fong et al., 2016; Meitinger et al., 2016; Meitinger et al., 2020; Yeow et al., 2020). In cells lacking centrosomes, TRIM37 loss accelerates acentrosomal spindle assembly, because it leads to the formation of an ectopic array of PLK4-scaffolded foci that recruit PCM proteins and can substitute for centrosomes in promoting spindle assembly in mitosis (Meitinger et al., 2016; Meitinger et al., 2020). A prominent component of these PLK4-scaffolded foci is the centrosomal component CEP192 (Fig. 9 A). To assess if centrobin is also present in the array of foci containing PLK4, CEP192, and other centrosomal components in cells lacking centrosomes, we analyzed centrobin localization in centrinone-treated *TRIM37Δ* cells. We found that the majority of PLK4 foci in centrinone-treated cells contained CEP192, but not centrobin, whereas one PLK4 focus contained centrobin and not CEP192 (Fig. 9 A). Thus, centrobin staining partitioned foci labeled with the PLK4 antibody in centrinone-treated *TRIM37Δ* cells into two types: a centrobin-containing focus (likely the highly ordered condensate described above) and an array of PLK4-containing foci that contain other centrosomal components such as CEP192, but not

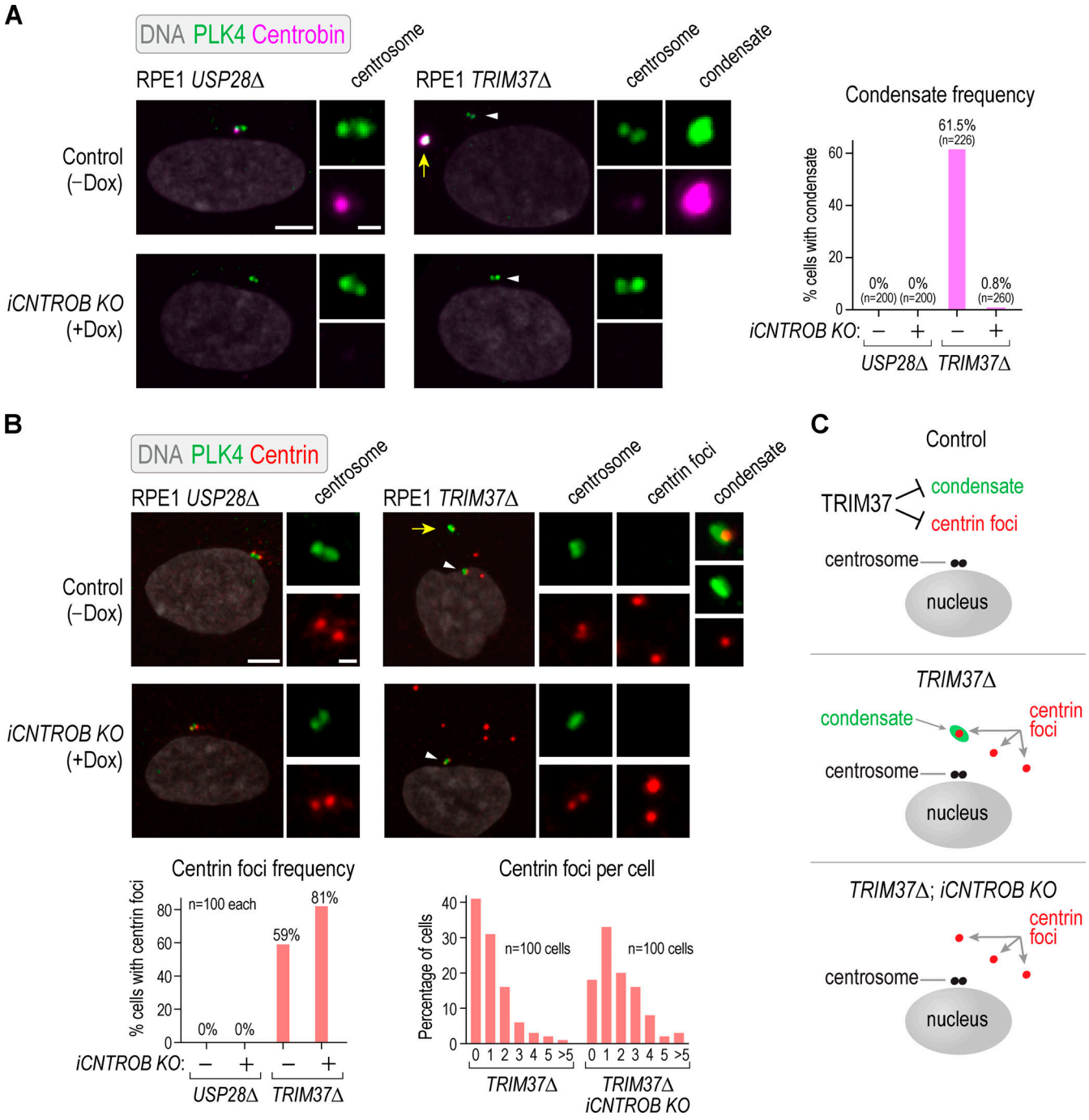

Figure 6. **Centrobin is required to form the condensate but not centrin-containing foci in *TRIM37Δ* cells. (A)** Localization of centrobin and PLK4 in the indicated conditions; centrosomes (white arrowheads) and condensates (yellow arrow) are indicated. The strategy to inducibly knock out *CNTROB* (*iCNTROB KO*) and efficacy of the knockout are shown in Fig. S3 A. Graph on the right plots frequency of condensates with and without addition of doxycycline to induce *CNTROB KO*. Scale bars, 5 µm and 1 µm (insets). Experiment was performed three times with similar results; data shown are from one experiment. **(B)** Localization of PLK4 and centrin in the indicated conditions; centrosomes (white arrowheads) and condensates (yellow arrow) are indicated. Graphs below plots the frequency of cells with centrin foci (left) and the number of centrin foci per cell (right). Scale bars, 5 µm and 1 µm (insets). Since *iCNTROB KO* is not 100% efficient, only cells that lacked centrosomal centrobin were quantified in the (+) condition in A and B. The experiment was performed once. **(C)** Schematics summarizing independent suppression of the condensate and centrin foci by TRIM37.

centrobin. Consistent with this partitioning, knockout of *CNTROB* eliminated the centrobin-scaffolded condensate in centrinone-treated *TRIM37Δ* cells but did not affect formation of PLK4-scaffolded foci (Fig. 9, B and C). By contrast, inducible *PLK4* knockout eliminated the PLK4-scaffolded foci, as shown previously (Meitinger et al., 2020), but the centrobin-containing condensate was still observed (Fig. 9, B and C). Thus, the array of PLK4-scaffolded foci in centrinone-treated *TRIM37Δ* cells

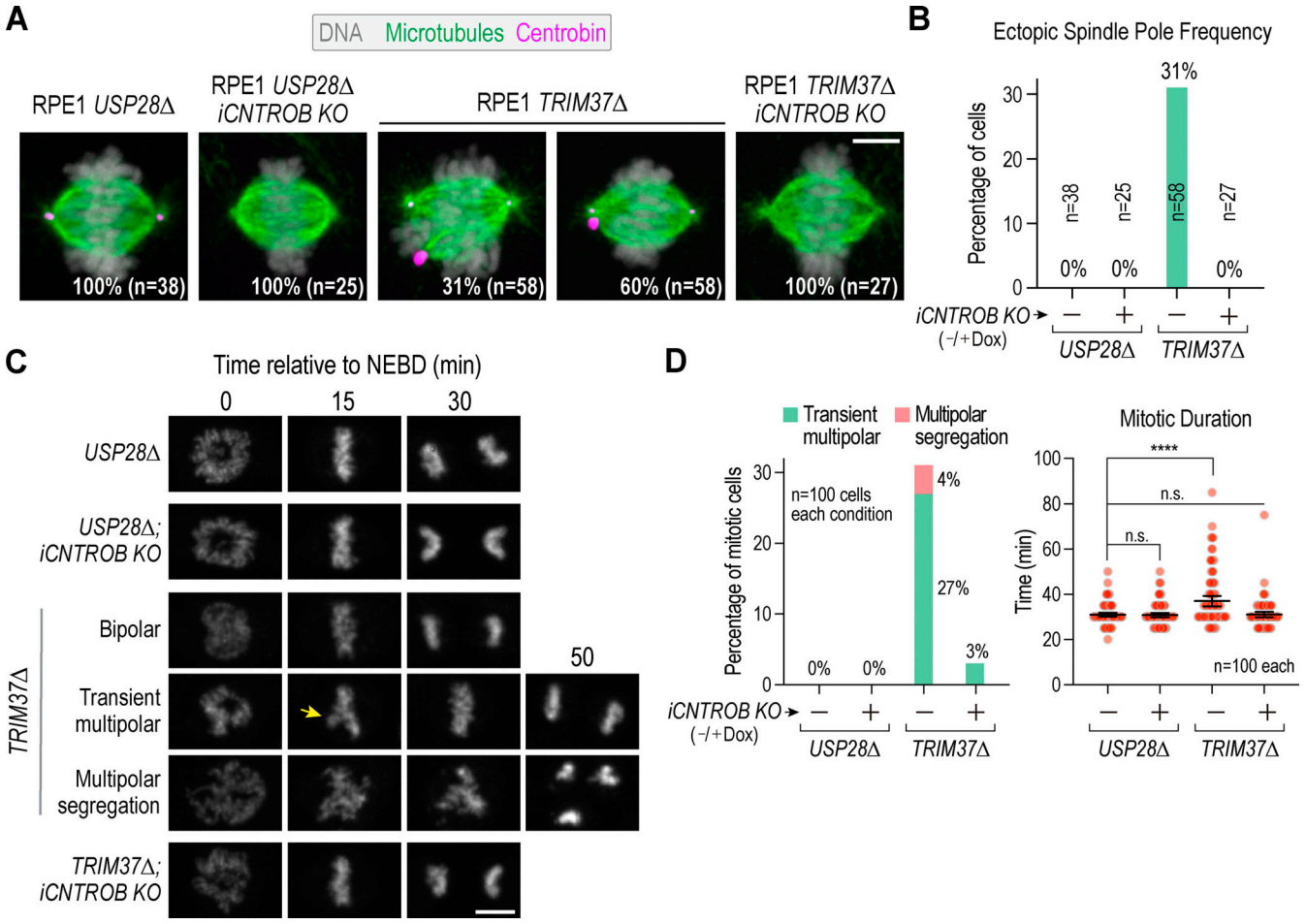

Figure 7. **Centrobin removal suppresses ectopic spindle pole formation in *TRIM37Δ* cells. (A)** Images of mitotic cells labeled for microtubules, centrobin, and DNA for the indicated conditions. Scale bar, 5 µm. **(B)** Quantification of ectopic spindle pole frequency for the indicated conditions. The experiment was performed once. **(C)** Stills from live imaging of mitotic chromosome dynamics for the indicated conditions; time 0 is nuclear envelope breakdown (NEBD). Transient multipolarity is evident in the chromosome configuration (arrow) in a subset of *TRIM37Δ* cells. Scale bar, 10 µm. **(D)** Quantification of transient multipolarity and multipolar segregation (left graph) and of mitotic duration (right graph), defined as the time from NEBD to chromosome decondensation. Mean and 95% CI for mitotic duration are plotted on top of the values for individual cells; P values are from unpaired *t* tests. The experiment shown in C was performed twice with similar outcomes; data from one experiment are quantified in D. ****, P < 0.0001.

that contain centrosomal components such as CEP192 is distinct from the structured centrobin-scaffolded condensate.

TRIM37 loss is proposed to improve mitosis in acentrosomal cells, because the PLK4-scaffolded foci act as efficient MTOCs that accelerate spindle assembly (Meitinger et al., 2016; Meitinger et al., 2020). In support of this idea, PLK4 knockout eliminated the functional improvement in spindle assembly, assessed by live imaging of chromosome dynamics, that is observed in centrinone-treated *TRIM37Δ* cells (Meitinger et al., 2020). We conducted the same analysis with *CNTROB* knockout, which does not affect the array of PLK4-scaffolded foci. The results showed that both in the presence and absence of centrobin, centrinone-treated *TRIM37Δ* cells exhibited significantly more efficient mitosis than centrinone-treated control *USP28Δ* cells (Fig. 9 D); in addition, PLK4-scaffolded foci were observed at the poles of the acentrosomal spindles with and without centrobin (Fig. 9 E). Thus, it is the PLK4-scaffolded foci and not the centrobin-scaffolded condensate that improve acentrosomal mitosis in centrinone-treated *TRIM37Δ* cells (Fig. 9 F).

We conclude that in cells that lack centrioles due to inhibition of PLK4 activity, TRIM37 prevents PLK4 protein from scaffolding the formation of centrobin-independent microtubule organizing foci that increase the efficiency of acentrosomal mitosis. This conclusion is consistent with the finding that TRIM37 interacts with and ubiquitinates PLK4 (Meitinger et al., 2020).

Discussion

Here, we investigate TRIM37 loss of function in cells that have centrosomes with the goal of defining cellular-level defects that underlie mulibrey nanism. Our results indicate that the major function of TRIM37 in dividing cells is to prevent the formation of a centrobin-scaffolded condensate (Fig. 10). These condensates frequently acquire the ability to serve as MTOCs after mitotic entry, which elevates chromosome missegregation (Fig. 10). TRIM37 loss also triggers the formation of foci containing the centriolar protein centrin. Removal of centrobin eliminates the condensates and the ectopic spindle poles in

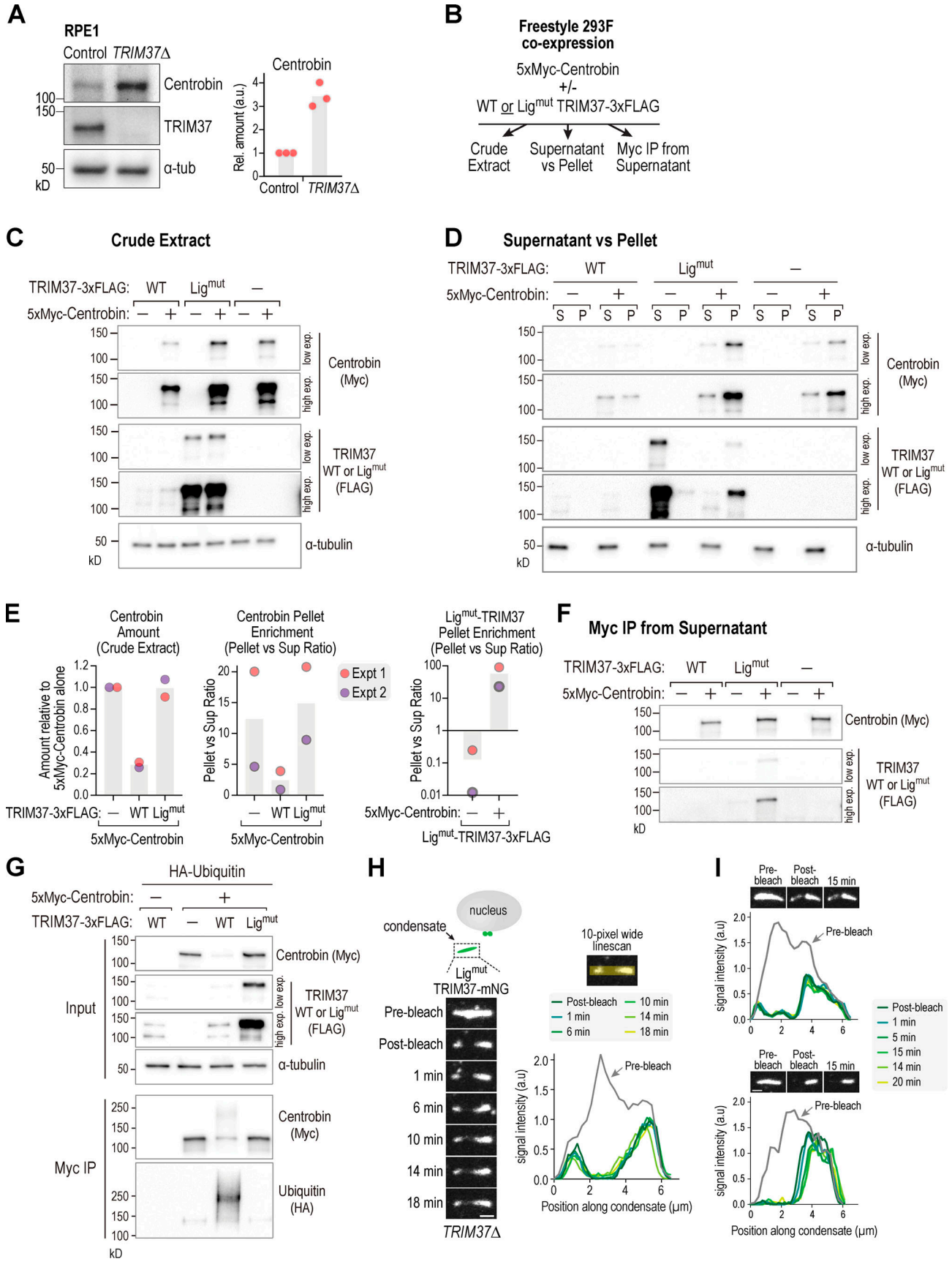

Figure 8. **TRIM37 interacts with and ubiquitinates centrobin. (A)** Immunoblotting of centrobin in the indicated cell lines. Graph on right plots centrobin levels relative to the mean control value (n = 3). **(B)** Schematic of coexpression-based analysis of regulation of centrobin by TRIM37 shown in C–G.

(C) Immunoblotting of crude extracts with the indicated antibodies. **(D)** Supernatant (S) and pellet (P) fractions immunoblotted with the indicated antibodies. α-tubulin fractionates into the supernatant, as expected for extracts prepared after cold treatment. Even under the denaturing conditions used, centrobin and Lig^{mut} TRIM37 were not consistently quantitatively recovered from the pellet. **(E)** Band signal intensity values from two independent experiments of total centrobin in crude extract (left), relative centrobin enrichment in pellet (middle), and relative Lig^{mut} TRIM37 enrichment in pellet; the Lig^{mut} TRIM37 pellet enrichment plot has a logarithmic y axis. Sup, supernatant. **(F)** Anti-Myc and Anti-FLAG immunoblotting of anti-Myc immunoprecipitates (IP). **(G)** Centrobin ubiquitination by TRIM37; a plasmid encoding HA-ubiquitin was included in the coexpression. The input shown is the crude extract. **(H and I)** FRAP analysis of Lig^{mut} TRIM37-mNG localized to condensates in *TRIM37Δ* cells. In H, multiple time point images and quantification of signal intensity along a 10-pixel-wide line is shown. The intensity value at the left most position before the condensate was used as the background and subtracted; after background subtraction, all pixel values were normalized by dividing by the average prebleach signal. In I, selected images are shown above the linescan plots. Images of the condensates from individual time-lapse movie frames were cropped and rotated before montaging. Scale bars, 1 µm. The experiment was performed five times with similar results; three examples are shown. α-Tubulin serves as a loading control in A, C, D, and G. high exp., higher exposure; low exp., lower exposure.

TRIM37Δ cells while leaving centrin-containing foci intact. Thus, centrobin-scaffolded condensates, and not centrin foci, underlie the mitotic defects of *TRIM37Δ* cells. We propose that low frequency chromosome missegregation is a prominent cellular-level defect underlying mulibrey nanism that additionally 1explains the tumor-prone nature of mulibrey patients (Fig. 10). The overlap in phenotypic features between mulibrey nanism and mosaic variegated aneuploidy (MVA), a distinct rare human genetic disorder associated with mitotic defects, lends support to this proposal.

TRIM37 limits the formation of centrosomal protein assemblies

A key function of TRIM37 is to prevent the formation of ectopic centrosomal protein assemblies that acquire the ability to serve as MTOCs. In acentrosomal cells generated by centrinone treatment, TRIM37 loss enables the formation of an array of PLK4-scaffolded foci that recruit centrosomal proteins and serve as MTOCs that substitute for centrosomes in spindle assembly (Meitinger et al., 2016; Meitinger et al., 2020). In cells with centrosomes, loss of TRIM37 leads to the formation of highly ordered centrobin-scaffolded condensate that can acquire MTOC activity and reduce the fidelity of bipolar mitosis. Identifying the specific sites in centrobin and PLK4 that are ubiquitinated by TRIM37 and dissecting the structure and assembly pathways for centrobin-scaffolded condensates and PLK4-scaffolded foci are important future goals.

Highly ordered centrobin-scaffolded condensates form in the absence of TRIM37

Centrobin-scaffolded condensates in *TRIM37Δ* cells are highly ordered and have either a linear striated or a hexagonally packed punctate sheet structure. Ectopic centrobin-containing structures with a striated morphology have also been reported in a recent study using RNAi-mediated TRIM37 depletion (Balestra et al., 2021). An important question raised by the highly ordered nature of these ectopic structures in *TRIM37Δ* cells and their formation at centrosomes is whether they reflect a normal assembly process in a specific biological context. As these assemblies are deleterious in mitotically dividing cells, we speculate that their formation may occur in a postmitotic context. Centrobin is highly expressed in testis (Lee et al., 2009; Liška et al., 2009; Zou et al., 2005), and analysis of a mutation in the *CNTROB* locus in rats suggests that it is involved in the process that shapes the spermatid head (Dunleavy et al., 2019; Liška et al., 2009). During spermatogenesis, centrobin localizes to a basket-like structure containing a parallel array of microtubules called the manchette that ensheaths the nucleus and to an actin- and keratin-5–based cytoskeletal plate called the acroplaxome that links the nuclear envelope to the inner membrane of the acrosome (Liška et al., 2009). Thus, one possibility is that TRIM37 controls the formation of these centrobin assemblies during spermatogenesis, explaining why the rat *CNTROB* locus mutant and *TRIM37* loss-of-function mutants in mice and humans are sterile.

Centrobin-scaffolded condensates in *TRIM37Δ* cells make ectopic spindle poles that elevate chromosome missegregation

Approximately one quarter of the centrobin-scaffolded condensates formed in *TRIM37Δ* cells recruit other centrosomal proteins and acquire the ability to serve as MTOCs upon mitotic entry. These condensate-based ectopic poles elevate chromosome missegregation in *TRIM37Δ* cells (Fig. 10). Notably, centrobin removal prevents condensate formation and eliminates ectopic spindle poles in *TRIM37Δ* cells. However, centrobin removal does not reduce the number of centrin-containing foci present in *TRIM37Δ* cells. We note that a recent study, which refers to the centrin foci as "Cenpas," suggested that they serve as MTOCs to form ectopic poles that contribute to genomic instability and that centrobin-scaffolded condensates may serve as platforms for the generation of Cenpas (Balestra et al., 2021). In contrast, the inducible *CNTROB* knockout analysis that we conducted in *TRIM37Δ* cells suggests that centrobin-scaffolded condensates rather than centrin foci/Cenpas are responsible for the observed spindle defects and argues against the idea that centrobin-scaffolded condensates are required to generate centrin foci/Cenpas. Addressing the functional significance of the centrin foci observed in *TRIM37Δ* cells will require a means for selectively eliminating them without affecting the centrobin-scaffolded condensate.

Why only a subset of centrobin-scaffolded condensates are activated to serve as mitotic MTOCs is currently unclear. In *Drosophila melanogaster* neuroblasts, centrobin has been implicated in assembly of a robust mitotic-like MTOC that forms during interphase around one of the two centrioles. In these cells, centrobin directs the recruitment of PCM components (including asterless and the PCM matrix protein Cnn) in a PLK1-regulated manner (Januschke et al., 2013). Like the *Drosophila* protein, human centrobin has also been shown to be phosphorylated

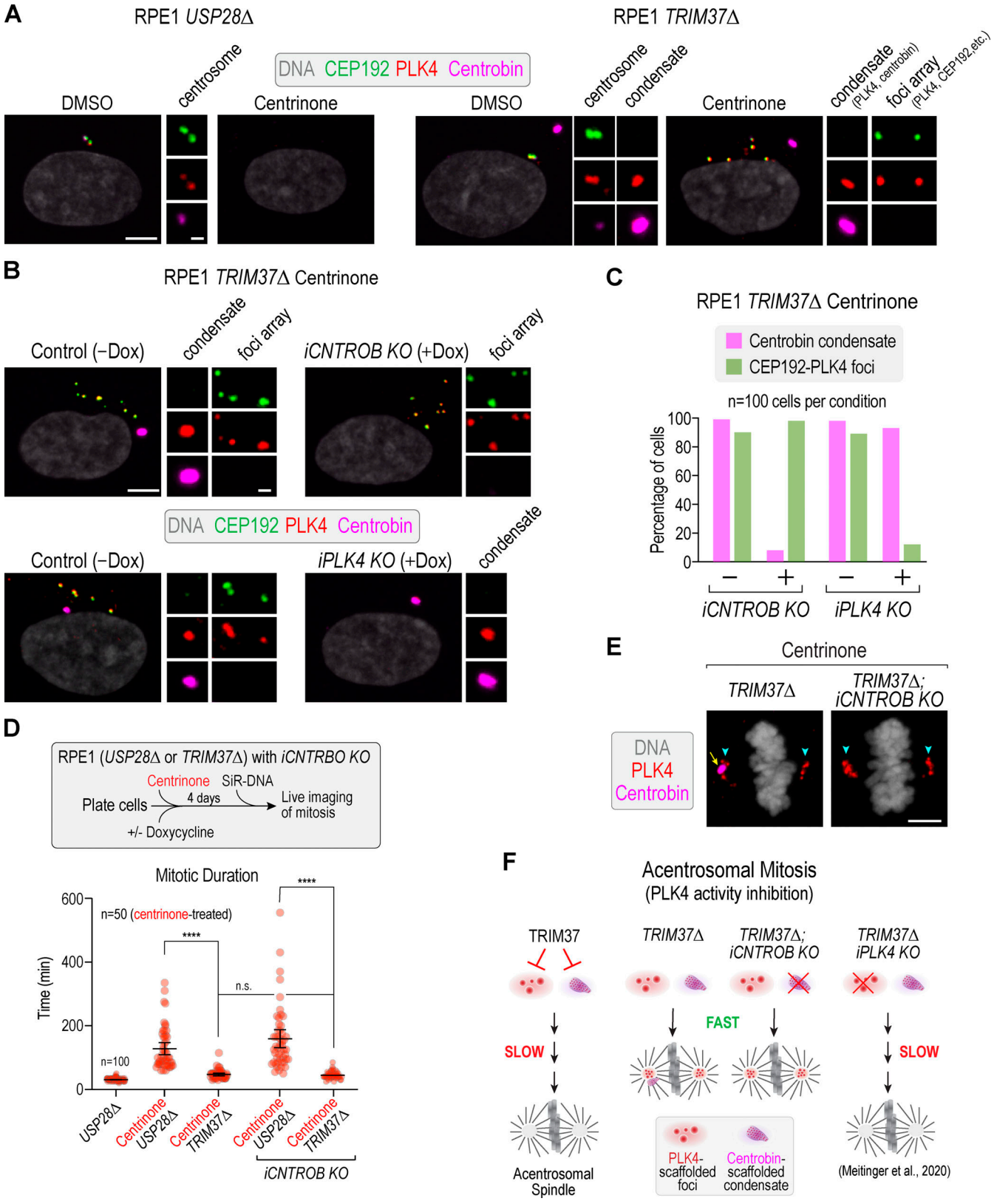

Figure 9. **PLK4-scaffolded foci that accelerate acentrosomal mitosis in *TRIM37Δ* cells are centrobin-independent. (A and B)** Immunostaining and fluorescent signal of in situ–tagged CEP192-mNG in *USP28Δ* and *TRIM37Δ* RPE1 cells treated with DMSO or centrinone (A) and additionally treated with doxycycline to induce *CNTROB* or *PLK4* knockout (B). Scale bars, 5 µm and 1 µm (insets). **(C)** Graph of the percentage of cells with condensates and CEP192-PLK4 foci in the indicated conditions. The experiment shown in A and B was performed twice with similar outcomes; data from one experiment are quantified in C. **(D)** Quantification of mitotic duration, measured as in Fig. 7 D, for the indicated conditions. Mean and 95% CI are plotted on top of the individual values;

P values are from *t* tests. ****, P < 0.0001. The experiment was performed twice with similar outcomes; data from one experiment are quantified. **(E)** Images of acentrosomal spindles in centrinone-treated *TRIM37Δ* cells, with and without centrobin. The centrobin-scaffolded condensate (yellow arrow) and the PLK4-scaffolded foci (cyan arrowheads) are marked. Scale bar, 5 µm. The experiment was performed twice with similar outcomes. **(F)** Schematic summary of analysis of acentrosomal mitosis following centrinone treatment. The PLK4-scaffolded foci, and not the centrobin-scaffolded condensate, improve acentrosomal mitosis following centrinone treatment.

by PLK1 during mitosis (Lee et al., 2010), suggesting that mitotic phosphorylation of centrobin by PLK1 may enable condensates to recruit other centrosomal components and acquire microtubule-nucleating capacity. As a significant proportion of condensates do not activate to become MTOCs in mitosis, there must be an additional step that is necessary.

TRIM37 mutation and mulibrey nanism: similarities to MVA?

TRIM37 loss leads to the formation of centrobin-scaffolded condensates that promote formation of multipolar spindles with elevated rates of chromosome missegregation. In RPE1 *TRIM37Δ* cells, the transient multipolar state resolves to a bipolar state before anaphase in the majority of cells but ∼5–6% of mitotic cells exhibit multipolar segregation and ∼2–3% exhibit lagging chromosomes (Fig. 10). Passage through a transient multipolar spindle intermediate elevates chromosome missegregation due to formation of merotelic kinetochore microtubule attachments in which a single kinetochore becomes attached to microtubules emanating from both spindle poles (Ganem et al., 2009; Silkworth et al., 2009). Thus, the ectopic spindle pole formed by the centrobin-scaffolded condensate in *TRIM37Δ* cells effectively act as a low-penetrance aneuploidy generator. We suggest that characteristics of mulibrey nanism, such as reduced pre- and postnatal growth and the high frequency of tumors (Karlberg et al., 2009a; Karlberg et al., 2009b; Sivunen et al., 2017), including Wilms' tumor, are a consequence of aneuploidy resulting from condensate-mediated multipolar spindle assembly. This notion is supported by analysis of mulibrey nanism patient-derived fibroblasts.

Slow pre- and postnatal growth and a high propensity for tumor formation, including Wilms' tumor, are also characteristic of patients with MVA (García-Castillo et al., 2008; Hanks et al., 2004; Snape et al., 2011; Yost et al., 2017). In these patients, >25% of cells have additional or missing chromosomes. MVA syndrome can result from mutations in *BUB1B* or *TRIP13*, which lead to defects in the spindle checkpoint and cause cells to exit

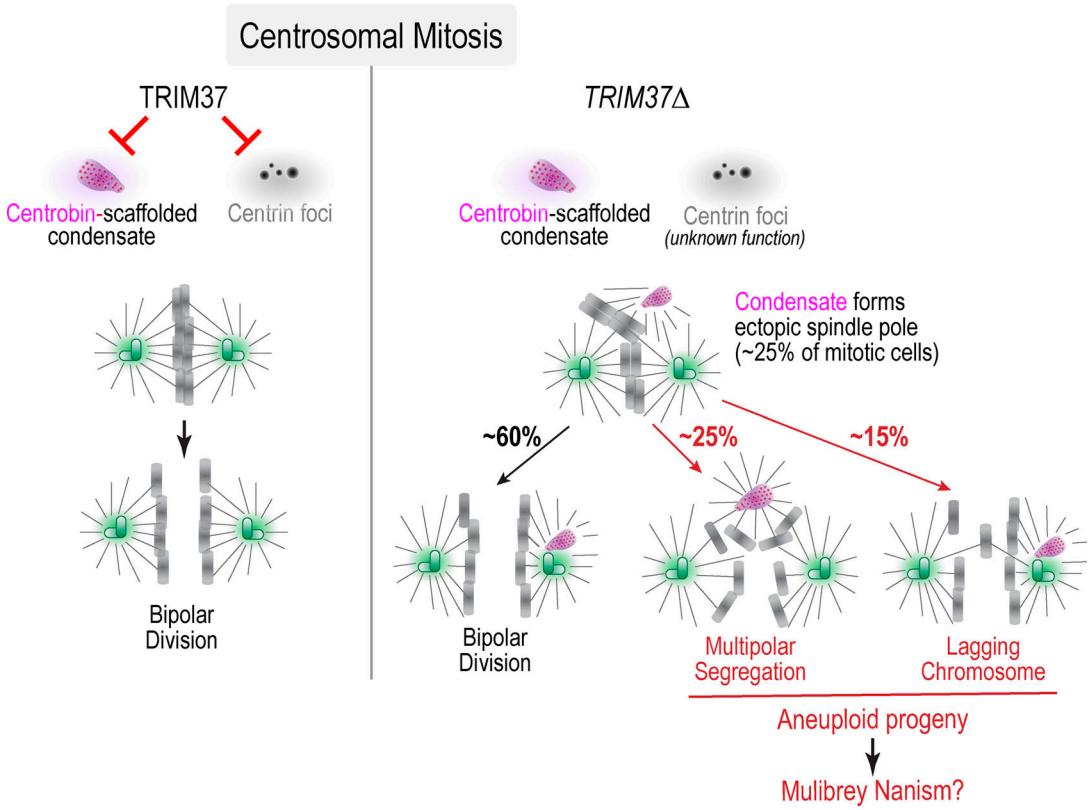

Figure 10. **Model for TRIM37 function in ensuring accurate chromosome segregation and its relevance to mulibrey nanism.** In the absence of TRIM37 activity, an ectopic centrobin-scaffolded condensate and centrin foci are formed. Approximately 25% of centrobin-scaffolded condensates assemble an ectopic spindle pole, resulting in both multipolar segregation and an elevated rate of lagging chromosomes. We propose that these low-frequency segregation errors caused by the centrobin-scaffolded ectopic spindle pole are major contributors to the pathology of mulibrey nanism. The centrin foci observed in *TRIM37Δ* cells are independent of the centrobin-scaffolded condensate; the functional impact of their formation remains to be elucidated.

mitosis before all chromosomes attach to the spindle (Hanks et al., 2004; Suijkerbuijk et al., 2010; Yost et al., 2017). The third described cause of MVA is mutations in the gene encoding the centrosomal protein CEP57 (Snape et al., 2011). *CEP57* mutation has been shown to disrupt the structure of the PCM matrix and cause precocious separation of mother and daughter centrioles (Aziz et al., 2018; Watanabe et al., 2019). Precociously separated daughter centrioles acquire the ability to serve as MTOCs before spindle assembly, leading to the formation of multipolar spindles (Aziz et al., 2018; Watanabe et al., 2019). Although patients with *CEP57* mutation–induced MVA are limited and not yet old enough to assess cancer susceptibility, mutation, loss, or haploinsuffiency of *CEP57* in mice rendered them susceptible to spontaneous and carcinogen-induced tumor formation (Aziz et al., 2018).

The similarities of the cellular and patient phenotypes resulting from mutations in *TRIM37* and *CEP57* lead us to propose that aneuploidy resulting from a centrobin-scaffolded condensate-dependent ectopic spindle pole explains many features of mulibrey nanism, including slow growth and susceptibility to tumor formation. We note that, as loss of TRIM37 perturbs the distribution of centrobin by rendering it largely insoluble, additional features of mulibrey nanism, such as infertility, may be related to disruption of centrobin function in gametes (Liška et al., 2009, 2013; Ogungbenro et al., 2018; Reina et al., 2018).

Materials and methods

Antibodies

Antibodies against CEP192 (1–211 aa; used at 0.5 µg/ml for immunofluorescence), SAS6 (501–657 aa; used at 0.5 µg/ml for immunofluorescence), and PLK4 (814–970 aa; used at 0.5 µg/ml for immunofluorescence) were generated as previously described (Wong et al., 2015). The following antibodies were purchased from commercial sources, with their working concentrations indicated in parentheses: anti-CENTROB (1:800 for immunofluorescence and Western blotting; 1:500 for expansion microscopy, STORM, and STED; ab70448; Abcam); anti-TRIM37 (1:2,000 for immunoblotting; A301-174A; Bethyl Laboratories); anti-CDK5RAP2 (1:1,000 for immunofluorescence; ab86340; Abcam); anti-Cep152 (1:1,000 ab183911; Abcam), anti-CEP152 (1:3,000; A302-479A; Bethyl Laboratories), anti-ARL13B (1:500; 17711-1-AP; Proteintech), anti–α-tubulin (1:500; T9026; Sigma-Aldrich), anti-PCNT (1:2,000 for immunofluorescence, 1:500 for immunoblotting; ab4448; Abcam), anti–γ-tubulin (T6557; 1:1,000; Sigma-Aldrich); anti–β-tubulin (1:500; ab15568; Abcam); anti-Centrin1 (1:1,000; 20H5; Millipore); anti-FLAG (1:1,000 for immunoblotting; F1804; Sigma-Aldrich); anti-Myc (1:5,000 for immunoblotting; monoclonal 9E10; M4439; Sigma-Aldrich); anti-HA (1:500 for immunoblotting; monoclonal antibody 16B12; BioLegend); anti-acetylated tubulin (1:4,000; T7451; Sigma-Aldrich); and anti-CEP290 (1:600; ab84870; Abcam). Anti-CENTROB and anti-Cep164 antibody (22227-1-AP; Proteintech) directly conjugated with CF647 using Mix-n-Stain CFDye antibody Labeling Kit (92238; Biotium) were used for costaining with anti α-tubulin and anti-CEP152 antibodies, respectively. Secondary antibodies for expansion microscopy anti-mouse Alexa Fluor 488 (1:800; A11029) and anti-rabbit Alexa Fluor 647 (1:800; A21245) were purchased from Thermo Fisher Scientific. In some expansion experiments, centrioles were visualized using anti-acetylated tubulin directly conjugated with CF568 using Mix-n-Stain CFDye antibody Labeling Kit (92235; Biotium). Other secondary antibodies were purchased from Jackson ImmunoResearch Laboratories and GE Healthcare.

Cell lines

All cell lines used in this study are listed in Table S1. RPE1 (hTERT RPE-1) cells were grown in F12/DMEM, and Lenti-X 293T cells were grown in DMEM. Both media were supplemented with 10% FBS. Fibroblast cell lines AG02602 (apparently healthy individual) and AG02506 (mulibrey nanism) were purchased from Coriell and grown in EMEM with 2 mM L-glutamine and 15% FBS. All media were supplemented with 100 µg/ml streptomycin and 100 U/ml penicillin. Cell lines were maintained in 37°C and 5% CO_2. FreeStyle 293-F cells were maintained at 37°C and 8% CO_2 on an orbital shaker platform rotating at 125 rpm. To inhibit PLK4 and deplete centrosomes, cells were treated with 150 nM centrinone (LCR-263; 150–200 nM; synthesized by Sundia MediTech) for the indicated amounts of time.

The RPE1 CEP192-NeonGreen and the RPE1 *TRIM37Δ* and *USP28Δ* knockout and inducible PLK4 knockout cell lines were described previously (Meitinger et al., 2016; Meitinger et al., 2020). The following transgenes were stably integrated into the genome using lentiviral constructs (see Table S2): mRuby2-MAP4-MBD (EF1α promoter; neomycin resistance gene), TRIM37-NeonGreen (hPGK promoter; blasticidin resistance gene), and TRIM37-C18R-NeonGreen (hPGK promoter; blasticidin resistance gene). Cell lines for inducible knockout of centrobin were generated by sequential lentiviral integration of Cas9 (Edit-R Inducible Lentiviral Cas9; Dharmacon) and a gRNA expressing plasmid, which is based on the lentiGuide-Puro plasmid (Sanjana et al., 2014). The centrobin gRNA (5′-GCT ACAGCAACAATTAGCCG-3′) targets exon 5. The lentiGuide-Puro was a gift from Feng Zhang (Massachusetts Institute of Technology, Cambridge, MA; plasmid 52963; http://n2t.net/addgene:52963; RRID:Addgene_52963; Addgene). Cas9 expression was induced with 1 µg/ml doxycycline.

Viral particles were generated by transfecting the lentiviral packaging constructs into Lenti-X-293T cells using Lenti-X Packaging Single Shots (Clontech). 48 h after transfection, virus-containing medium was harvested and added to the growth medium of cells in combination with polybrene (8 µg/ml; EMD Millipore). Cells were selected for 1 wk in 400 µg/ml G418, 5 µg/ml blasticidin, or 10 µg/ml puromycin.

Expansion microscopy

Expansion microscopy analysis was performed as described previously (Kong et al., 2020; Sahabandu et al., 2019). The protocol yielded a fourfold expansion of the specimen. Briefly, cells growing on glass coverslips were fixed with 4% formaldehyde in PBS at RT for 1 h. After fixation, the coverslips were incubated at 40°C for 16 h in a solution containing 30%

acrylamide (A4058; Sigma-Aldrich) and 4% formaldehyde in PBS. Cells were washed three times in PBS (10 min each wash at RT). Coverslips were placed on a parafilm-covered Petri dish floating in an ice-water bath. Precooled gelling mixture consisting of 20% acrylamide, 0.04% bis-acrylamide (A9926; Sigma-Aldrich), 7% sodium acrylate (408220; Sigma-Aldrich), 0.5% ammonium persulfate (248614; Sigma-Aldrich), and 0.5% tetramethylethylenediamine (411019; Sigma-Aldrich) was pipetted onto the coverslips, incubated on ice for 20 min, and additionally at RT for 1–2 h. Following gel polymerization, several punches were excised from each gelled sample using a 4-mm biopsy puncher (33–34-P/25; Integra Miltex). Punches were placed in a dry 50-ml tube and preheated at >90°C for 10 min. SDS solution (200 mM SDS, 200 mM NaCl, and 50 mM Tris, pH 9.0), preheated to >90°C, was added to the punches, which were boiled for 1 h at >90°C with swirling of the tube every 10 min. After boiling, SDS solution containing punches was cooled to RT, and SDS was removed by exchanging 1× PBS every 20 min for the first 2–3 h, followed by an overnight wash in 1× PBS at 4°C.

Punches were blocked in immunofluorescence (IF) buffer containing 1% BSA (A9647; Sigma-Aldrich) and 0.05% Tween-20 (P9416; Sigma-Aldrich) in PBS for 1 h at RT and incubated with primary antibody diluted in IF buffer for 48 h at 4°C. Punches were washed in PBS for 1 h and incubated with secondary antibody and 0.5 µg/ml DAPI (D1306; Thermo Fisher Scientific) in IF buffer for 24 h at 4°C. After immunostaining, samples were expanded in deionized water (dH_2O) for 2 h at RT with dH_2O exchanged every 10 min and additionally overnight at 4°C. Prior to imaging, expanded punches were mounted in Rose chambers (Kong and Loncarek, 2015; Rose, 1954).

Widefield images of expanded samples were acquired on inverted Eclipse Ti microscope (Nikon), equipped with Orca-Flash4 camera (Hamamatsu), Intensilight C-HGFIE illuminator, 60× NA 1.45 Plan Apo objective, and 1.5× magnifying tube lens. One central Z section or multiple 200- to 300-nm-thick Z sections spanning the centriole or the entire cell were acquired, as needed.

SIM of expanded samples was performed on N-SIM (Nikon), equipped with 405-, 488-, 561-, and 640-nm excitation lasers, Apo TIRF 100× NA 1.49 Plan Apo oil objective, and a back-illuminated electron-multiplying charge-coupled device (CCD) camera (DU897; Andor). 0.1-µm Z sections were acquired in 3D SIM mode and reconstructed to generate a final SIM image. Nikon NIS Elements software was used for surface rendering.

In the expanded samples, G1 cells were recognized by the presence of two unduplicated centrioles and S phase cells by two closely positioned duplicated centrioles. G2 cells were identified by two separated and duplicated centrioles. Prophase cells were identified by DNA condensation within the nucleus. Various stages of mitosis were recognized by characteristic DNA morphology.

Analysis and assembly of expansion microscopy images was performed in Photoshop (Adobe) and Fiji (National Institutes of Health). To improve the visibility of the dimmer signals and when quantitative differences between fluorescent signals were not critical, the levels of fluorescent signals were sometimes differentially adjusted between different image panels. Maximum intensity projections of multiple Z slices were presented. To illustrate centriole width, length, and number, only the central Z section through a centriole was presented.

The length of acetylated signal of mother centrioles in horizontal orientation in G1, S, and G2 phases were measured along longitudinal axes at half-width half maxima on both centriole ends (Kong et al., 2020). To determine the distance between striations of expanded centrobin-rich aggregates, the distance between the fluorescent maxima between two stripes or adjacent puncta was measured. The same strategy was used to determine the distance between adjacent stripes from STED and STORM images.

Immunolabeling for STORM and STED

Cells were fixed in 1.5% formaldehyde for 4 min at RT and postfixed in methanol for 4 min at −20°C. Cells were washed in 1×PBS for 30 min and incubated with IF buffer (1% BSA and 0.05% Tween-20) for 15 min. Samples were incubated in primary anti-CENTROB or anti-PLK4 antibodies overnight at 4°C. Following the wash in 1×PBS, samples were incubated with anti-mouse or anti-rabbit antibodies conjugated with CF647 (20042 and 20045; Biotium) diluted to 1:800 in IF buffer for STORM. Anti-mouse or anti-rabbit secondary antibodies conjugated with Abberior STAR RED (STRED-1001 and STRED-1002; Abberioir) diluted to 1:200 in IF buffer were used for STED.

STORM

Before STORM imaging, coverslips were mounted in Attofluor Cell chambers (A7816; Thermo Fisher Scientific) and layered with 100-nm tetra-spectral fluorescent microspheres (T7279; Thermo Fisher Scientific), which served as fiducial markers. Samples were imaged in STORM buffer consisting of 25 mM β-mercaptoethylamine (30070; Sigma-Aldrich), 0.5 mg/ml glucose oxidase (G2133; Sigma-Aldrich), 67 µg/ml catalase (C40; Sigma-Aldrich), and 10% dextrose (D9434; Sigma-Aldrich) in 100 mM Tris, pH 8.0. 3D STORM imaging was performed on Nikon N-STORM4.0 system using an Eclipse Ti2 inverted microscope; a super resolution high power Apo TIRF 100× NA 1.49 oil objective; 405-, 561-, and 647-nm excitation laser launch; and a back-illuminated electron-multiplying CCD camera (DU897; Andor). The 647-nm laser line (~150 mW at the fiber and ~90 mW before the objective lens) was used to promote fluorophore blinking. The 405-nm laser was used to activate fluorophores. The signals of fiducial markers were recorded using a 561-nm laser. 20,000 to 30,000 time points were acquired every 20 ms at a 50-Hz frame rate. NIS Elements (Nikon) was used to analyze the data.

Prior to STORM imaging, the position of the CF647-labeled target protein (PLK4 and centrobin) was recorded in a widefield mode. A rainbow Z-color-coding scheme was used for signal presentation. The signals closer to the coverslip were presented in red and those further from the coverslip in blue, typically spanning 650 nm of a working Z imaging range. The original Z-color-coding scheme was preserved on image panels. 3D STORM data are presented as a projection of the entire 3D volume.

STED

Coverslips with immunolabeled cells were mounted in a homemade mounting medium (90% glycerol, 100 mM Tris, pH 8.0, and 0.1 mg/ml p-phenylenediamine; 695106; Sigma-Aldrich). 2D STED imaging was performed using STEDYCON (Abberior Instruments) assembled on Eclipse Ti2 inverted microscope (Nikon), 100× NA 1.45 Plan Apo objective. Avalanche photo detectors (650–700 nm, 575–625 nm, and 505–545 nm; DAPI detection) were used to detect the signals. Browser based control software (Abberior Instruments) was used to generate STED images.

FRAP

RPE1 *TRIM37Δ* TRIM37-C18R-mNG cells grown on glass coverslips were mounted in Attofluor Cell chambers (A7816; Thermo Fisher Scientific) in CO_2 Independent Medium (Gibco). FRAP experiments were conducted on a custom-assembled workstation centered around an inverted Eclipse Ti microscope (Nikon), equipped with a back-illuminated electron multiplying CCD camera (DU888; Andor); 100× NA 1.45 Plan Apo objective, Yokogawa spinning disk (Yokogawa Electric Corporation); 405-, 488-, 561-, and 640-nm laser launch (MLC400; Agilent); and a 2× relay lens. A 488-nm photobleaching laser (OBIS 488-nm LX 30 mW; Coherent) was run at 20-Hz repetition rate. Collimated laser beam was attenuated, delivered through back epi-port of the microscope and expanded to fill the back aperture of the objective. One or two ∼200-ms laser pulses were used to bleach the fluorescent signals. Before and immediately after bleaching, fluorescence images were recorded in a confocal mode collecting 0.2-µm Z sections. Recovery of the fluorescent signal was recorded by acquiring images at 1-min time intervals.

CLEM

CLEM analysis was performed as previously described (Kong and Loncarek, 2015). RPE1 *TRIM37Δ* TRIM37-C18R-mNG cells grown on glass coverslip were first imaged using a confocal microscope, and 200-nm-thick Z sections through the entire volume of a target cell were recorded to register the position of TRIM37-C18R-mNG containing condensates in the cell. A fixative consisting of 2.5% glutaraldehyde (G5882; Sigma-Aldrich) and 0.25% formaldehyde (15686; Electron Microscopy Sciences) in PBS (pH 7.4) was added to the cells, and the position of the condensate was recorded again after fixation. Differential interference contrast (DIC) images were acquired to determine the position of the condensate in the cell. Samples were fixed for additional 1 h at RT, washed in PBS for 30 min (10 min each wash), prestained with 1% osmium tetroxide (19100; Electron Microscopy Sciences) and 1% uranyl acetate (22400; Electron Microscopy Sciences), dehydrated in graded ethanol series, and then embedded in EMbed-812 resin (13940; Electron Microscopy Sciences). 80-nm serial sections of the target cells were sectioned, placed on the formvar-coated copper grids (2330P-XA; SPI Supplies), and further contrasted with uranyl acetate and lead citrate. Imaging was performed using a FEI Spirit transmission electron microscope, operating at 80 kV. The analysis and alignment of the serial sections and image analysis and was performed in Adobe Photoshop and Fiji.

To measure the distance between electron-dense stripes and puncta in striated and punctuated aggregates, the distance between centers of adjacent electron-dense regions were measured from electron micrographs.

Immunofluorescence and quantification of centrosomal signals

For immunofluorescence, 10,000 cells per well were seeded into 96-well plates 1 d before fixation. Cells were fixed in 100 µl ice-cold methanol for 7 min at −20°C. Cells were washed twice with washing buffer (PBS containing 0.1% Triton X-100) and blocked with blocking buffer (PBS containing 2% BSA, 0.1% Triton X-100, and 0.1% NaN_3) overnight. After blocking, cells were incubated for 2 h with primary antibody in fresh blocking buffer (concentrations as indicated above). Cells were washed three times with washing buffer before 1-h incubation with the secondary antibody and DNA staining Hoechst 33342 dye. Finally, cells were washed three times with washing buffer before inspection. Images were acquired on a CV7000 spinning-disk confocal system (Yokogawa Electric Corporation) equipped with a 40× (0.95 NA) or a 60× (water, 1.2 NA) U-Plan Apo objective and a 2,560 × 2,160 pixel scientific complementary metal oxide seminconductor (sCMOS) camera (Andor). Image acquisition was performed using CV7000 software.

Live-cell imaging

Live-cell imaging was performed on the CQ1 spinning-disk confocal system (Yokogawa Electric Corporation) equipped with a 40× 0.95 NA U-Plan Apo objective and a 2,560 × 2,160 pixel sCMOS camera (Andor) at 37°C and 5% CO_2. Image acquisition and data analysis were performed using CQ1 and Fiji software, respectively.

Cells were seeded into 96-well polystyrene plates at 10,000 cells/well 24 h before imaging unless indicated otherwise. Imaging conditions varied according to the experimental setup. For imaging SiR-DNA, 5 × 2-µm Z sections in the RFP or FarRed channel (25% power, 150 ms) were acquired in each field at 5-min intervals for 6–24 h. The DNA marker SiR-DNA was added 2 h before imaging at a working concentration of 0.5 µM. For live imaging of TRIM37-mNG and mRuby-MAP4-MBD, 8 × 1.2-µm Z sections in the GFP and/or RFP channel (50% power, 150 ms) were acquired in each field at 4- to 15-min intervals for 6–12 h. DMSO or centrinone treatment was conducted for three cell cycles before start of imaging, unless noted otherwise.

Immunoblotting

For immunoblotting experiments shown in Fig. 8 A, a similar number of asynchronously growing cells were harvested from 6-well dishes with 2× Laemmli SDS sample buffer at 80–90% confluence and lysed by sonication. For every sample, ∼10–30 µg protein/lane was run on Mini-PROTEAN gels (Bio-Rad) and transferred to polyvinylidene difluoride (PVDF) membranes using a TransBlot Turbo system (Bio-Rad). Blocking and antibody incubations were performed in TBS-T + 5% nonfat dry milk. Detection was performed using HRP-conjugated secondary antibodies (GE Healthcare) with WesternBright Sirius (Advansta) or SuperSignal West Femto (Thermo Fisher Scientific)

substrates. Membranes were imaged on a ChemiDoc MP system (Bio-Rad).

Microtubule regrowth

10,000 cells per well were seeded into 96-well plates on the day before the experiment. The plate was incubated for 40 min on ice to depolymerize the microtubules. The plate was then transferred to RT, and the medium was replaced with 200 µl prewarmed (37°C) medium. After 1-min incubation, cells were fixed with 100 µl ice-cold methanol and incubated for 5 min at −20°C. Immunostaining was performed as described above.

FISH

For FISH, 250,000 cells per well were seeded into a 6-well plate with 18-mm coverslips 1 d before analysis. Cells were washed with 2 ml PBS and then fixed with Carnoy's fixative (methanol/acetic acid = 3:1) for 15 min at RT. Plates were then stored overnight at −20°C. For each coverslip, 5 µl probe (Metasystem XCE 17 green and XCE 18 green) was applied and covered with a slide. The samples and probes were then denatured by heating the slides on a 75°C hot plate for 2 min, sealed with rubber cement, and incubated at 37°C in a humidified chamber overnight. The next day, coverslips were washed with 0.4× SCC at 72°C for 2 min, RT 2× SCC and 0.05% Tween-20 for 30 s PBS. Coverslips were then incubated with DAPI (1:1,000 in PBS) for 10 min and washed with PBS for 1 min. Each coverslip was sealed on a slide with 20 µl anti-fade solution (ProLong Gold; Thermo Fisher Scientific) and stored at 4°C in the dark. 12 × 200 nm Z sections in the DAPI (80% power, 500 ms) and GFP channel (80% power, 500 ms) were acquired with a CQ1 spinning-disk confocal system (Yokogawa Electric Corporation) equipped with a 40× 0.95 NA U-Plan Apo objective and a 2,560 × 2,160 pixel sCMOS camera (Andor). Image acquisition and data analysis were performed using CQ1 and Fiji software, respectively.

Protein expression in FreeStyle 293-F cells, immunoprecipitation, and detection of centrobin ubiquitination

For immunoprecipitation assays, FLAG-tagged TRIM37 and Myc-tagged centrobin (see Table S2) were expressed in the FreeStyle 293-F cells (Thermo Fisher Scientific). The empty 5Myc plasmid (CS2P #17095; Addgene) or 3FLAG plasmid (p3XFLAG-CMV-7.1, E7533; Sigma-Aldrich) were used as negative controls. Cell transfection was performed using FreeStyle MAX Reagent and OptiPRO SFM according to the manufacturer's guidelines (Thermo Fisher Scientific). 20 ml of cells at 10^6 cells/ml were transfected with a total of 25 µg DNA constructs. 43–48 h after transfection, cells were harvested and washed with PBS. For MG132 treatment, 10 µM MG132 (M8699; Sigma-Aldrich) was added 6 h before harvesting the cells. The cells were resuspended in lysis buffer (20 mM Tris/HCl, pH 7.5, 150 mM NaCl, 1% Triton X-100, 5 mM EGTA, 1 mM DTT, 2 mM $MgCl_2$ and EDTA-free protease inhibitor cocktail; Roche) and lysed in an ice-cold sonicating water bath for 5 min. Crude extract was taken right after the sonication and suspended in SDS sample buffer. After 15-min centrifugation at 15,000 ×*g*. at 4°C, the whole-cell lysates were separated to supernatant and pellet and taken for the cosedimentation assay. The rest of supernatant was incubated with Pierce Anti-c-Myc magnetic beads (Thermo Fisher Scientific) for 2 h at 4°C. The beads were washed five times with lysis buffer and resuspended in SDS sample buffer. For immunoblotting, equal volumes of samples were run on Mini-PROTEAN gels (Bio-Rad) and transferred to polyvinylidene fluoride membranes using a TransBlot Turbo system (Bio-Rad). Blocking and antibody incubations were performed in TBS-T plus 5% nonfat dry milk or in TBS-T plus 5% BSA. Immunoblotting was performed as described above.

To detect ubiquitination of centrobin by TRIM37, FreeStyle 293-F cells were transfected as described above with DNA constructs encoding Myc-tagged centrobin, HA-tagged ubiquitin, and FLAG-tagged TRIM37, and cells were harvested after 48 h. The plasmid encoding HA-ubiquitin was a gift from Edward Yeh (University of Missouri, Columbia, MO; plasmid 18712; http://n2t.net/addgene:18712; RRID:Addgene_18712; Addgene). Cells were lysed in 20 mM Tris/HCl, pH 7.5, 150 mM NaCl, 1% Triton X-100, 5 mM EGTA, 1 mM DTT, 2 mM $MgCl_2$, EDTA-free protease inhibitor cocktail (Roche), and 5 mM N-ethylmaleimide, and immunoprecipitation and immunoblotting were performed as described above.

Statistical analysis

Statistical analysis was conducted using Prism v8 (GraphPad). P values were determined by *t* tests. Unpaired *t* tests assuming equal standard deviation were performed (Fig. 1, C and G; Fig. 7 D; Fig. 9 D; Fig. S1 A; Fig. S3 B; and Fig. S4 B; ns, $P > 0.05$; *, $P < 0.05$; **, $P < 0.01$; ***, $P < 0.001$; ****, $P < 0.0001$).

Online supplemental material

Fig. S1 shows the centrosomal localization of TRIM37 and further characterization of the condensates in *TRIM37Δ* cells. Fig. S2 shows centrosomal component localization to centrobin condensates at ectopic spindle poles and nucleation activity of mitotic condensates in a microtubule repolymerization experiment. Fig. S3 shows the strategy used to engineer inducible *CNTROB* knockout and knockout validation by genotyping and centrosome immunofluorescence. Fig. S4 shows the immunofluorescence analysis of the inducible *PLK4* knockout and of centrin in the inducible *CNTROB* knockout. Fig. S5 shows some additional coexpression analysis of the regulation of centrobin by TRIM37. Video 1 shows the birth of a condensate in TRIM37Δ RPE1 cells expressing the condensate marker Lig^{mut}-TRIM37-mNG and the microtubule-binding domain of MAP4 fused to mRuby2. Video 2 shows spindle assembly in control (*USP28Δ*) and *TRIM37Δ* RPE1 cells expressing the microtubule-binding domain of MAP4 fused to mRuby2. Video 3 shows *TRIM37Δ* RPE1 cells expressing an mNG fusion of WT or ligase mutant (C18R) TRIM37 and a fusion of mRuby2 with the microtubule-binding domain of MAP4. Video 4 shows chromosomes labeled with SiR-DNA in control (*USP28Δ*) and *TRIM37Δ* RPE1 cells with and without induced centrobin knockout. Video 5 shows the recovery after photobleaching of condensates in *TRIM37Δ* RPE1 cells expressing Lig^{mut}-TRIM37-mNG. Table S1 lists the human cell lines used in this study. Table S2 lists the plasmids used in this study.

Acknowledgments

We thank A. Shiau and D. Jenkins for imaging support, J. Anzola for help with coexpression analysis in FreeStyle 293F cells, and O. Shoshani for help with FISH.

This work was supported by grants from the National Institutes of Health to K. Oegema (GM074207) and A. Desai (GM074215). F. Meitinger received support from the German Science Foundation (ME 4713/1-1). M. Ohta was supported by the Japan Society for the Promotion of Science. J. Loncarek was supported by the Intramural Research Program of the National Institutes of Health, National Cancer Institute. A. Desai and K. Oegema received salary support from the Ludwig Institute for Cancer Research.

The authors declare no competing financial interests.

Author contributions: The study was conceptualized by K. Oegema, A. Desai, and J. Loncarek. F. Meitinger engineered cell lines and conducted immunofluorescence and live imaging experiments. D. Kong and J. Loncarek conducted the CLEM, expansion, STORM, and STED analyses. M. Ohta conducted coexpression-based biochemical experiments. J. Loncarek and M. Ohta conducted the photobleaching analysis. The manuscript draft was prepared by A. Desai, K. Oegema, and J. Loncarek and finalized with input from F. Meitinger, D. Kong, and M. Ohta.

Submitted: 31 October 2020
Revised: 25 February 2021
Accepted: 6 April 2021

References

Avela, K., M. Lipsanen-Nyman, N. Idänheimo, E. Seemanová, S. Rosengren, T.P. Mäkelä, J. Perheentupa, A.D. Chapelle, and A.E. Lehesjoki. 2000. Gene encoding a new RING-B-box-Coiled-coil protein is mutated in mulibrey nanism. *Nat. Genet.* 25:298–301. https://doi.org/10.1038/77053

Aziz, K., C.J. Sieben, K.B. Jeganathan, M. Hamada, B.A. Davies, R.O.F. Velasco, N. Rahman, D.J. Katzmann, and J.M. van Deursen. 2018. Mosaic-variegated aneuploidy syndrome mutation or haploinsufficiency in Cep57 impairs tumor suppression. *J. Clin. Invest.* 128:3517–3534. https://doi.org/10.1172/JCI120316

Balestra, F.R., P. Strnad, I. Flückiger, and P. Gönczy. 2013. Discovering regulators of centriole biogenesis through siRNA-based functional genomics in human cells. *Dev. Cell.* 25:555–571. https://doi.org/10.1016/j.devcel.2013.05.016

Balestra, F.R., A. Domínguez-Calvo, B. Wolf, C. Busso, A. Buff, T. Averink, M. Lipsanen-Nyman, P. Huertas, R.M. Ríos, and P. Gönczy. 2021. TRIM37 prevents formation of centriolar protein assemblies by regulating Centrobin. *eLife.* 10:e62640. https://doi.org/10.7554/eLife.62640

Banterle, N., and P. Gönczy. 2017. Centriole Biogenesis: From Identifying the Characters to Understanding the Plot. *Annu. Rev. Cell Dev. Biol.* 33:23–49. https://doi.org/10.1146/annurev-cellbio-100616-060454

Breslow, D.K., and A.J. Holland. 2019. Mechanism and Regulation of Centriole and Cilium Biogenesis. *Annu. Rev. Biochem.* 88:691–724. https://doi.org/10.1146/annurev-biochem-013118-111153

Brigant, B., V. Metzinger-Le Meuth, J. Rochette, and L. Metzinger. 2018. TRIMming down to TRIM37: Relevance to Inflammation, Cardiovascular Disorders, and Cancer in MULIBREY Nanism. *Int. J. Mol. Sci.* 20:67. https://doi.org/10.3390/ijms20010067

Brinkman, E.K., T. Chen, M. Amendola, and B. van Steensel. 2014. Easy quantitative assessment of genome editing by sequence trace decomposition. *Nucleic Acids Res.* 42:e168. https://doi.org/10.1093/nar/gku936

de Bie, P., and A. Ciechanover. 2011. Ubiquitination of E3 ligases: self-regulation of the ubiquitin system via proteolytic and non-proteolytic mechanisms. *Cell Death Differ.* 18:1393–1402. https://doi.org/10.1038/cdd.2011.16

Dunleavy, J.E.M., M.K. O'Bryan, P.G. Stanton, and L. O'Donnell. 2019. The cytoskeleton in spermatogenesis. *Reproduction.* 157:R53–R72. https://doi.org/10.1530/REP-18-0457

Firat-Karalar, E.N., N. Rauniyar, J.R. Yates III, and T. Stearns. 2014. Proximity interactions among centrosome components identify regulators of centriole duplication. *Curr. Biol.* 24:664–670. https://doi.org/10.1016/j.cub.2014.01.067

Fong, C.S., G. Mazo, T. Das, J. Goodman, M. Kim, B.P. O'Rourke, D. Izquierdo, and M.F. Tsou. 2016. 53BP1 and USP28 mediate p53-dependent cell cycle arrest in response to centrosome loss and prolonged mitosis. *eLife.* 5:e16270. https://doi.org/10.7554/eLife.16270

Ganem, N.J., S.A. Godinho, and D. Pellman. 2009. A mechanism linking extra centrosomes to chromosomal instability. *Nature.* 460:278–282. https://doi.org/10.1038/nature08136

García-Castillo, H., A.I. Vásquez-Velásquez, H. Rivera, and P. Barros-Núñez. 2008. Clinical and genetic heterogeneity in patients with mosaic variegated aneuploidy: delineation of clinical subtypes. *Am. J. Med. Genet. A.* 146A:1687–1695. https://doi.org/10.1002/ajmg.a.32315

Hanks, S., K. Coleman, S. Reid, A. Plaja, H. Firth, D. Fitzpatrick, A. Kidd, K. Méhes, R. Nash, N. Robin, et al. 2004. Constitutional aneuploidy and cancer predisposition caused by biallelic mutations in BUB1B. *Nat. Genet.* 36:1159–1161. https://doi.org/10.1038/ng1449

Januschke, J., J. Reina, S. Llamazares, T. Bertran, F. Rossi, J. Roig, and C. Gonzalez. 2013. Centrobin controls mother-daughter centriole asymmetry in Drosophila neuroblasts. *Nat. Cell Biol.* 15:241–248. https://doi.org/10.1038/ncb2671

Kallijärvi, J., K. Avela, M. Lipsanen-Nyman, I. Ulmanen, and A.E. Lehesjoki. 2002. The TRIM37 gene encodes a peroxisomal RING-B-box-coiled-coil protein: classification of mulibrey nanism as a new peroxisomal disorder. *Am. J. Hum. Genet.* 70:1215–1228. https://doi.org/10.1086/340256

Karlberg, N., S. Karlberg, R. Karikoski, S. Mikkola, M. Lipsanen-Nyman, and H. Jalanko. 2009a. High frequency of tumours in Mulibrey nanism. *J. Pathol.* 218:163–171. https://doi.org/10.1002/path.2538

Karlberg, S., M. Lipsanen-Nyman, H. Lassus, J. Kallijärvi, A.E. Lehesjoki, and R. Butzow. 2009b. Gynecological tumors in Mulibrey nanism and role for RING finger protein TRIM37 in the pathogenesis of ovarian fibrothecomas. *Mod. Pathol.* 22:570–578. https://doi.org/10.1038/modpathol.2009.13

Kettunen, K.M., R. Karikoski, R.H. Hämäläinen, T.T. Toivonen, V.D. Antonenkov, N. Kulesskaya, V. Voikar, M. Hölttä-Vuori, E. Ikonen, K. Sainio, et al. 2016. Trim37-deficient mice recapitulate several features of the multi-organ disorder Mulibrey nanism. *Biol. Open.* 5:584–595. https://doi.org/10.1242/bio.016246

Kong, D., and J. Loncarek. 2015. Correlative light and electron microscopy analysis of the centrosome: A step-by-step protocol. *Methods Cell Biol.* 129:1–18. https://doi.org/10.1016/bs.mcb.2015.03.013

Kong, D., N. Sahabandu, C. Sullenberger, A. Vasquez-Limeta, D. Luvsanjav, K. Lukasik, and J. Loncarek. 2020. Prolonged mitosis results in structurally aberrant and over-elongated centrioles. *J. Cell Biol.* 219:e201910019.

Lee, J., S. Kim, Y. Jeong, and K. Rhee. 2009. Centrobin/Nip2 expression in vivo suggests its involvement in cell proliferation. *Mol. Cells.* 28:31–36. https://doi.org/10.1007/s10059-009-0097-9

Lee, J., Y. Jeong, S. Jeong, and K. Rhee. 2010. Centrobin/NIP2 is a microtubule stabilizer whose activity is enhanced by PLK1 phosphorylation during mitosis. *J. Biol. Chem.* 285:25476–25484. https://doi.org/10.1074/jbc.M109.099127

Liška, F., C. Gosele, E. Rivkin, L. Tres, M.C. Cardoso, P. Domaing, E. Krejcí, P. Snajdr, M.A. Lee-Kirsch, D.G. de Rooij, et al. 2009. Rat hd mutation reveals an essential role of centrobin in spermatid head shaping and assembly of the head-tail coupling apparatus. *Biol. Reprod.* 81:1196–1205. https://doi.org/10.1095/biolreprod.109.078980

Liška, F., C. Gosele, E. Popova, B. Chylíková, D. Křenová, V. Křen, M. Bader, L.L. Tres, N. Hubner, and A.L. Kierszenbaum. 2013. Overexpression of full-length centrobin rescues limb malformation but not male fertility of the hypodactylous (hd) rats. *PLoS One.* 8:e60859. https://doi.org/10.1371/journal.pone.0060859

Loncarek, J., and M. Bettencourt-Dias. 2018. Building the right centriole for each cell type. *J. Cell Biol.* 217:823–835. https://doi.org/10.1083/jcb.201704093

Meitinger, F., J.V. Anzola, M. Kaulich, A. Richardson, J.D. Stender, C. Benner, C.K. Glass, S.F. Dowdy, A. Desai, A.K. Shiau, and K. Oegema. 2016. 53BP1 and USP28 mediate p53 activation and G1 arrest after centrosome loss or extended mitotic duration. *J. Cell Biol.* 214:155–166. https://doi.org/10.1083/jcb.201604081

Meitinger, F., M. Ohta, K.Y. Lee, S. Watanabe, R.L. Davis, J.V. Anzola, R. Kabeche, D.A. Jenkins, A.K. Shiau, A. Desai, and K. Oegema. 2020. TRIM37 controls cancer-specific vulnerability to PLK4 inhibition. *Nature.* 585:440–446. https://doi.org/10.1038/s41586-020-2710-1

Mennella, V., D.A. Agard, B. Huang, and L. Pelletier. 2014. Amorphous no more: subdiffraction view of the pericentriolar material architecture. *Trends Cell Biol.* 24:188–197. https://doi.org/10.1016/j.tcb.2013.10.001

Ogungbenro, Y.A., T.C. Tena, D. Gaboriau, P. Lalor, P. Dockery, M. Philipp, and C.G. Morrison. 2018. Centrobin controls primary ciliogenesis in vertebrates. *J. Cell Biol.* 217:1205–1215. https://doi.org/10.1083/jcb.201706095

Park, H.H. 2018. Structure of TRAF Family: Current Understanding of Receptor Recognition. *Front. Immunol.* 9:1999. https://doi.org/10.3389/fimmu.2018.01999

Reina, J., M. Gottardo, M.G. Riparbelli, S. Llamazares, G. Callaini, and C. Gonzalez. 2018. Centrobin is essential for C-tubule assembly and flagellum development in *Drosophila melanogaster* spermatogenesis. *J. Cell Biol.* 217:2365–2372. https://doi.org/10.1083/jcb.201801032

Rose, G. 1954. A separable and multipurpose tissue culture chamber. *Tex. Rep. Biol. Med.* 12:1074–1083.

Sahabandu, N., D. Kong, V. Magidson, R. Nanjundappa, C. Sullenberger, M.R. Mahjoub, and J. Loncarek. 2019. Expansion microscopy for the analysis of centrioles and cilia. *J. Microsc.* 276:145–159. https://doi.org/10.1111/jmi.12841

Sanjana, N.E., O. Shalem, and F. Zhang. 2014. Improved vectors and genome-wide libraries for CRISPR screening. *Nat. Methods.* 11:783–784. https://doi.org/10.1038/nmeth.3047

Silkworth, W.T., I.K. Nardi, L.M. Scholl, and D. Cimini. 2009. Multipolar spindle pole coalescence is a major source of kinetochore mis-attachment and chromosome mis-segregation in cancer cells. *PLoS One.* 4:e6564. https://doi.org/10.1371/journal.pone.0006564

Sivunen, J., S. Karlberg, J. Lohi, N. Karlberg, M. Lipsanen-Nyman, and H. Jalanko. 2017. Renal findings in patients with Mulibrey nanism. *Pediatr. Nephrol.* 32:1531–1536. https://doi.org/10.1007/s00467-017-3669-5

Snape, K., S. Hanks, E. Ruark, P. Barros-Núñez, A. Elliott, A. Murray, A.H. Lane, N. Shannon, P. Callier, D. Chitayat, et al. 2011. Mutations in CEP57 cause mosaic variegated aneuploidy syndrome. *Nat. Genet.* 43:527–529. https://doi.org/10.1038/ng.822

Suijkerbuijk, S.J., M.H. van Osch, F.L. Bos, S. Hanks, N. Rahman, and G.J. Kops. 2010. Molecular causes for BUBR1 dysfunction in the human cancer predisposition syndrome mosaic variegated aneuploidy. *Cancer Res.* 70:4891–4900. https://doi.org/10.1158/0008-5472.CAN-09-4319

Wang, W., Z.J. Xia, J.C. Farré, and S. Subramani. 2017. TRIM37, a novel E3 ligase for PEX5-mediated peroxisomal matrix protein import. *J. Cell Biol.* 216:2843–2858. https://doi.org/10.1083/jcb.201611170

Watanabe, K., D. Takao, K.K. Ito, M. Takahashi, and D. Kitagawa. 2019. The Cep57-pericentrin module organizes PCM expansion and centriole engagement. *Nat. Commun.* 10:931. https://doi.org/10.1038/s41467-019-08862-2

Wong, Y.L., J.V. Anzola, R.L. Davis, M. Yoon, A. Motamedi, A. Kroll, C.P. Seo, J.E. Hsia, S.K. Kim, J.W. Mitchell, et al. 2015. Reversible centriole depletion with an inhibitor of Polo-like kinase 4. *Science.* 348:1155–1160. https://doi.org/10.1126/science.aaa5111

Woodruff, J.B., O. Wueseke, and A.A. Hyman. 2014. Pericentriolar material structure and dynamics. *Philos. Trans. R. Soc. Lond. B Biol. Sci.* 369:20130459. https://doi.org/10.1098/rstb.2013.0459

Yeow, Z.Y., B.G. Lambrus, R. Marlow, K.H. Zhan, M.A. Durin, L.T. Evans, P.M. Scott, T. Phan, E. Park, L.A. Ruiz, et al. 2020. Targeting TRIM37-driven centrosome dysfunction in 17q23-amplified breast cancer. *Nature.* 585:447–452. https://doi.org/10.1038/s41586-020-2690-1

Yost, S., B. de Wolf, S. Hanks, A. Zachariou, C. Marcozzi, M. Clarke, R. de Voer, B. Etemad, E. Uijttewaal, E. Ramsay, et al. 2017. Biallelic TRIP13 mutations predispose to Wilms tumor and chromosome mis-segregation. *Nat. Genet.* 49:1148–1151. https://doi.org/10.1038/ng.3883

Zou, C., J. Li, Y. Bai, W.T. Gunning, D.E. Wazer, V. Band, and Q. Gao. 2005. Centrobin: a novel daughter centriole-associated protein that is required for centriole duplication. *J. Cell Biol.* 171:437–445. https://doi.org/10.1083/jcb.200506185

JCB

Supplemental material

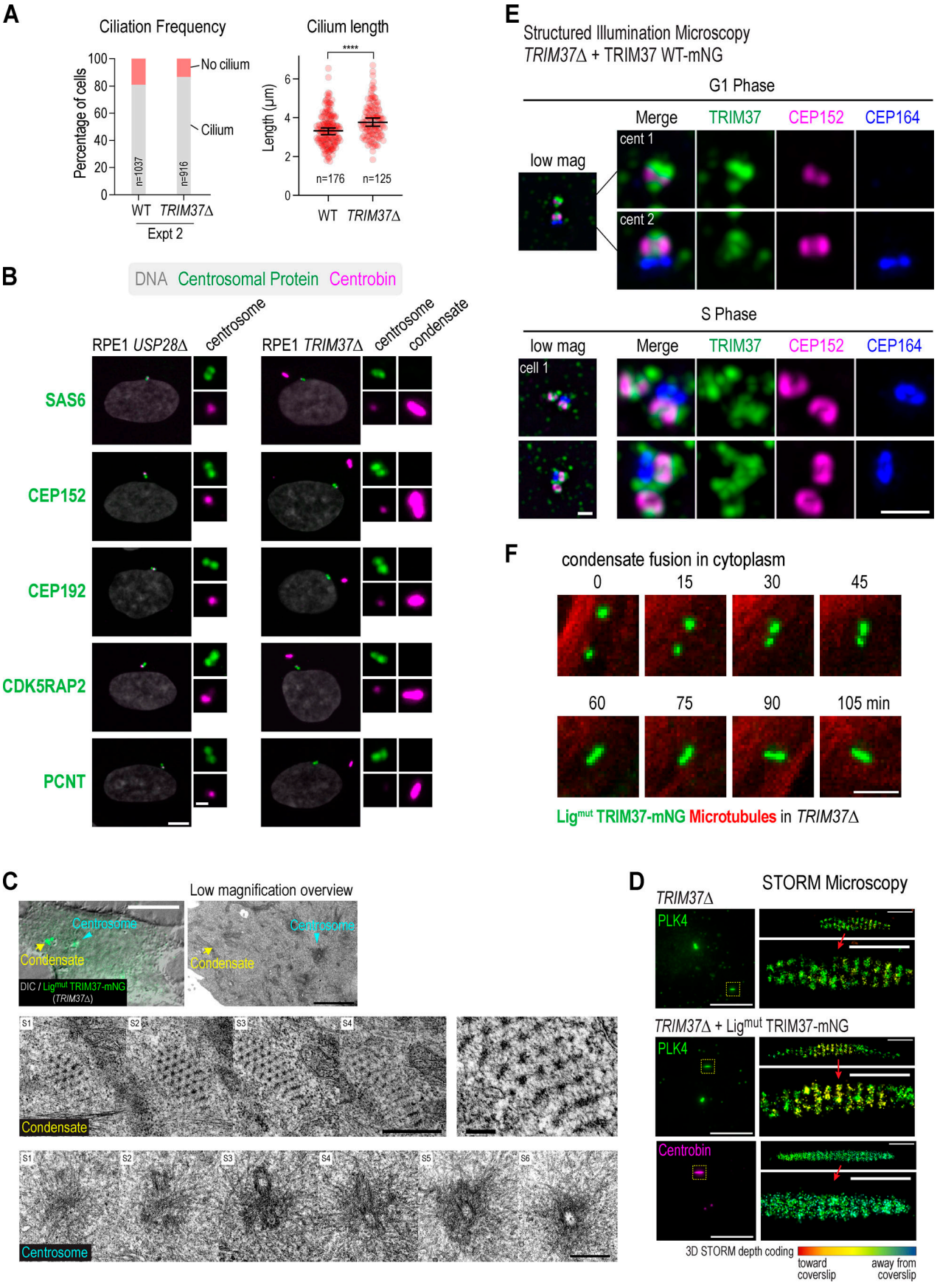
A
Ciliation Frequency
Percentage of cells
No cilium
Cilium
n=1037
n=916
WT
TRIM37Δ
Expt 2
Cilium length
Length (µm)
****
n=176
n=125
WT
TRIM37Δ
B
DNA Centrosomal Protein Centrobin
RPE1 USP28Δ
centrosome
RPE1 TRIM37Δ
centrosome
condensate
SAS6
CEP152
CEP192
CDK5RAP2
PCNT
C
Low magnification overview
Centrosome
Condensate
DIC / Ligmut TRIM37-mNG (TRIM37Δ)
Centrosome
Condensate
S1
S2
S3
S4
Condensate
S1
S2
S3
S4
S5
S6
Centrosome
D
STORM Microscopy
TRIM37Δ
PLK4
TRIM37Δ + Ligmut TRIM37-mNG
PLK4
Centrobin
3D STORM depth coding
toward coverslip
away from coverslip
E
Structured Illumination Microscopy
TRIM37Δ + TRIM37 WT-mNG
G1 Phase
low mag
Merge
TRIM37
CEP152
CEP164
cent 1
cent 2
S Phase
low mag
cell 1
Merge
TRIM37
CEP152
CEP164
F
condensate fusion in cytoplasm
0
15
30
45
60
75
90
105 min
Ligmut TRIM37-mNG Microtubules in TRIM37Δ

Figure S1. **Analysis of TRIM37 localization and additional characterization of phenotypes of *TRIM37Δ* RPE1 cells. (A)** Independent experiment analyzing ciliation frequency (left) and quantification of primary cilium length (right). n, number of cells analyzed; median and 95% CI are shown on top of individual data points in the right graph. The experiment was performed twice, the first experiment in triplicate and the second experiment in duplicate, with similar results; ciliation frequency and cilium length quantified from the second experiment are shown here, and ciliation frequency from the first experiment is shown in Fig. 1 E. **(B)** Immunofluorescence of centrobin and the indicated centrosomal components in *USP28Δ* and *TRIM37Δ* RPE1 cells. Scale bars, 5 µm (1 µm in insets). The experiment was performed once. **(C)** Expanded view of CLEM analysis of the cell shown in Fig. 2 B. Additional serial sections of the condensate and centrosome, a low-magnification EM view, and a higher-magnification view of the condensate are shown along with replication of the images shown in Fig. 2 B. White scale bar, 20 µm. Black scale bars: low magnification view, 2 µm; condensate and centrosome serial sections, 0.5 µm; zoomed-in view of punctate sheet condensate, 0.1 µm. **(D)** 3D STORM of condensates labeled with centrobin or PLK4. Reference widefield images are on the left. The STORM images are color coded for depth. Scale bars, 10 µm (widefield), 0.5 µm (STORM). Experiment performed twice with similar results; images are from one experiment. Red arrows indicate that the images on the bottom are higher magnification views of the corresponding regions of the images on top. **(E)** TRIM37-mNG localization at centrosomes visualized using SIM. CEP152 marks the proximal end of centrioles. CEP164 marks the distal end of the mother centriole. TRIM37 is broadly localized to the centrosome; it does not concentrate in a specific subdomain. Scale bars, 1 µm. The experiment was performed twice with similar results; images are from one experiment. mag, magnification. **(F)** Rare example of condensate fusion observed by live imaging of Lig^{mut} TRIM37-mNG expressed in *TRIM37Δ* cells. The fused condensate retains an elongated shape. Scale bar, 5 µm.

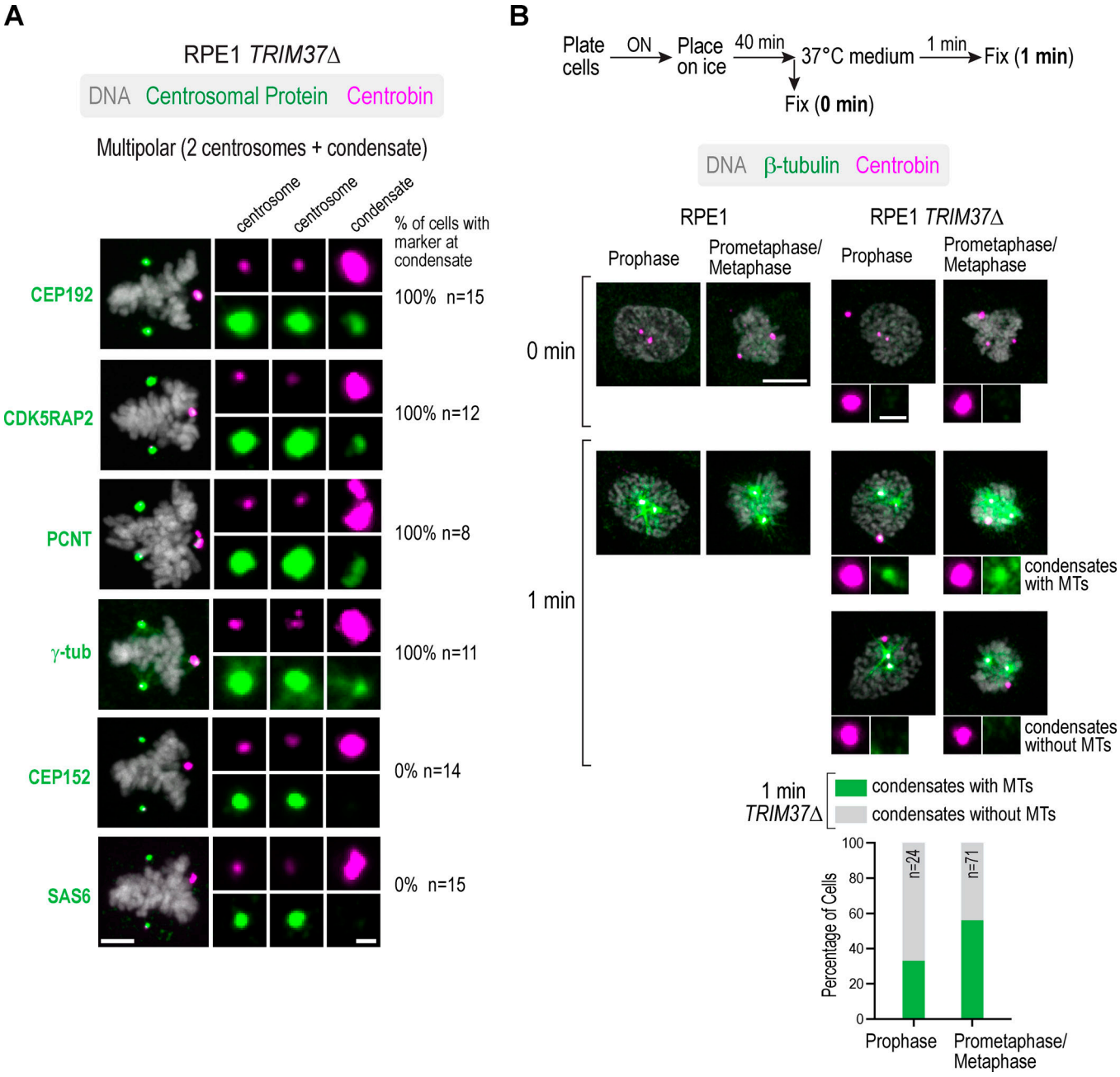

Figure S2. **Analysis of centrosomal component localization to centrobin condensate-based ectopic spindle poles and microtubule nucleation activity of mitotic condensates following microtubule depolymerization. (A)** Analysis of centrosomal component localization in mitotic *TRIM37Δ* cells with an ectopic condensate-based spindle pole. Scale bars, 5 µm and 1 µm (insets). **(B)** Microtubule regrowth analysis comparing control RPE1 and *TRIM37Δ* RPE1 mitotic cells. The protocol used for this analysis is schematized on the top. Cells were plated overnight (ON), chilled on ice for 40 min, and fixed (0 min) or warmed with 37°C medium for 1 min and then fixed (1 min). Example images of prophase and prometaphase/metaphase stage cells for the 0-min and 1-min conditions are shown. In mitotic *TRIM37Δ* cells, condensates that nucleated microtubules and condensates that did not were both observed; quantification of the ability of condensates in *TRIM37Δ* cells to nucleate microtubules after 1 min rewarming is plotted below the images. Scale bars, 10 µm and 2 µm (insets). The experiment was performed once.

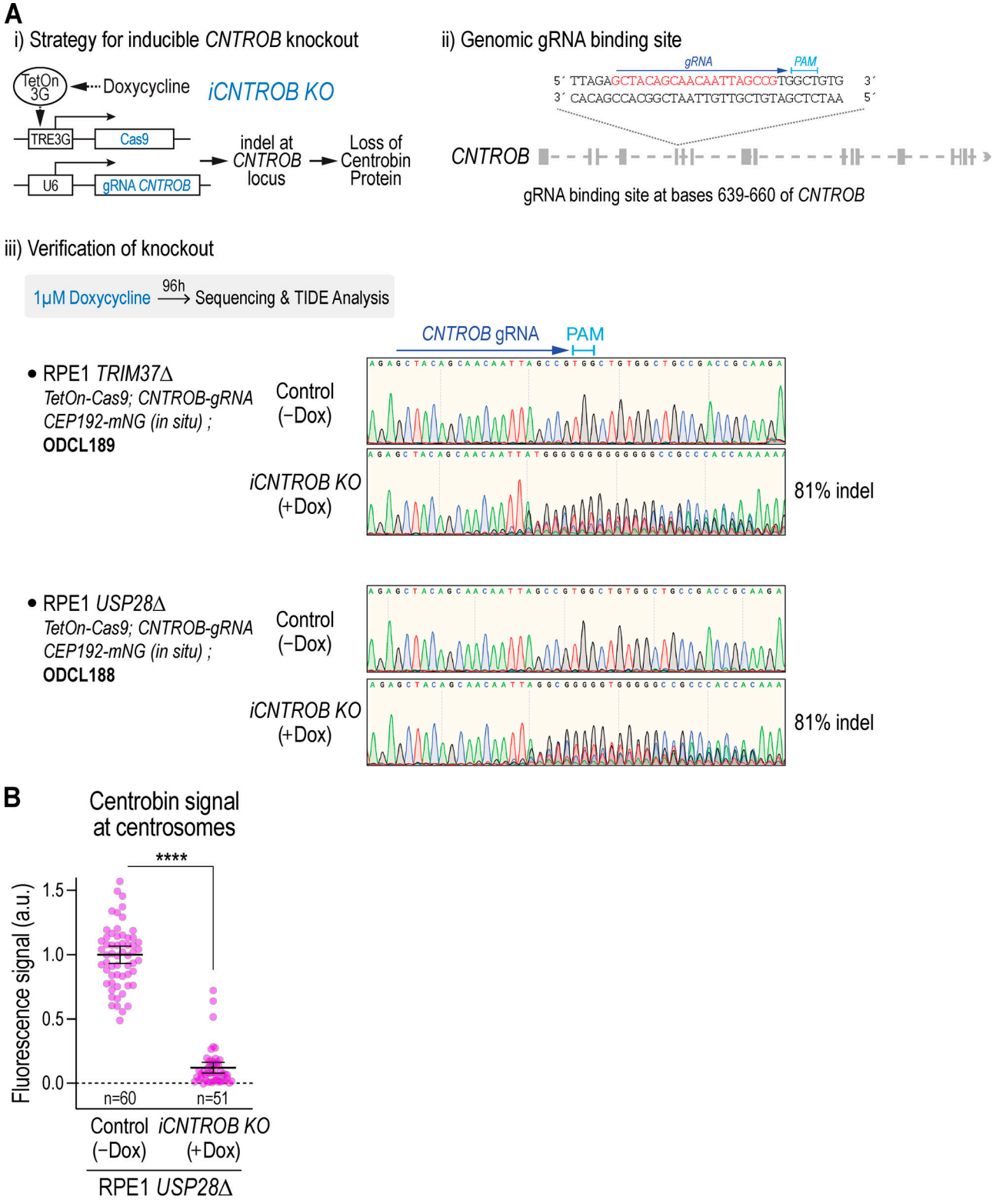

Figure S3. **Strategy used to engineer inducible *CNTROB* knockout and validation of knockout by genotyping and centrosome immunofluorescence.** **(A)** Strategy used to engineer *iCNTROB KO* in *TRIM37Δ* and *USP28Δ* RPE1 cells (i) and details of the *CNTROB* gRNA, indicating target site in the *CNTROB* locus (ii). Note that both cell lines have in situ mNG-tagged CEP192. To validate the efficacy of the knockout, tracking of indels by decomposition (TIDE) analysis (Brinkman et al., 2014) was conducted 4 d after induction with 1 μM doxycycline. In both cell lines, ∼80% indels were observed in the induced population. **(B)** Quantification of centrobin signal at centrosomes 4 d after induction of the knockout. Mean and 95% CI are plotted on top of measurements of individual centrosome pairs (the signal for both centrosomes in a cell was measured together); P value is from an unpaired *t* test. Experiment performed twice; data shown is from one experiment.

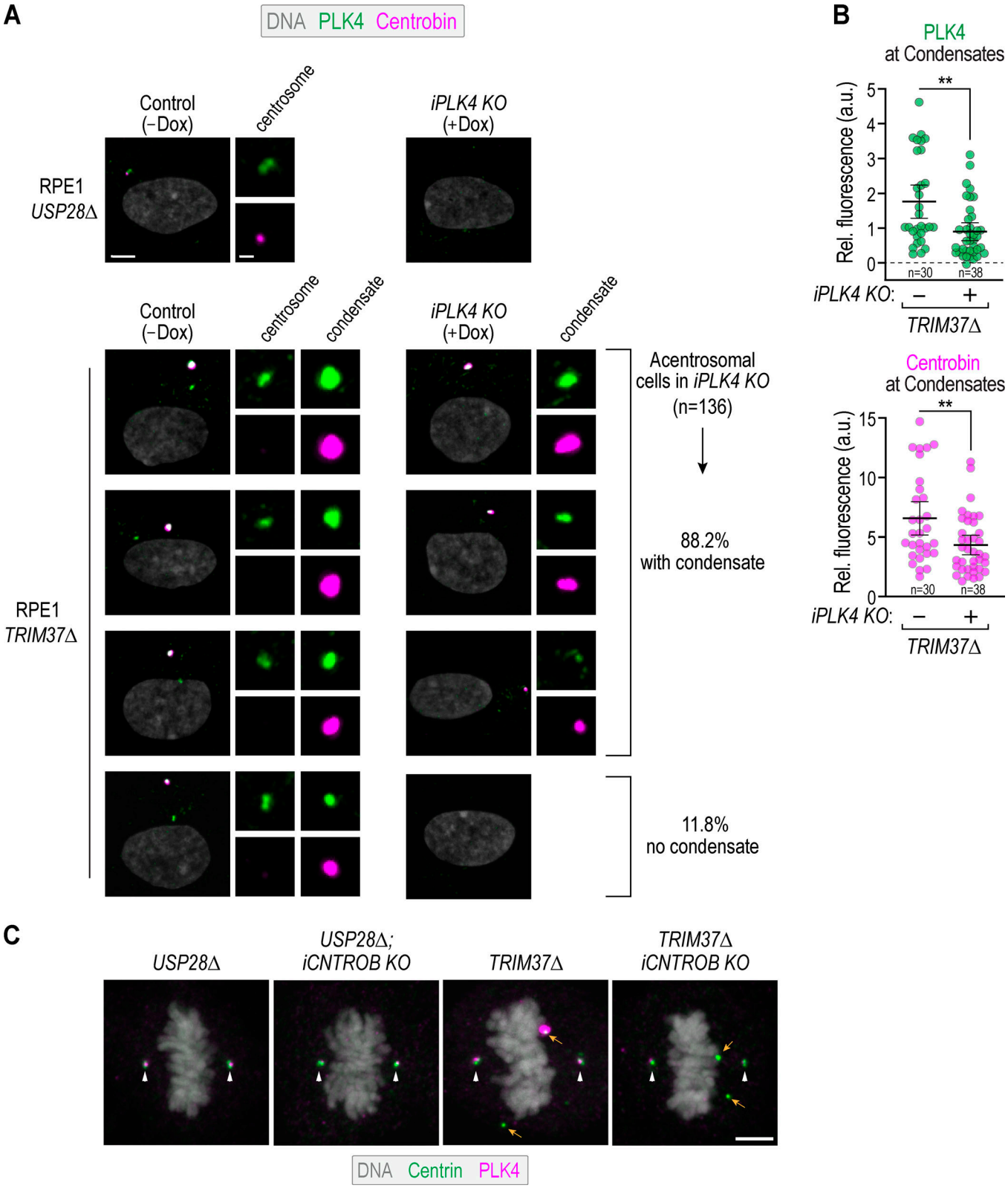

Figure S4. **Analysis of the inducible *PLK4* knockout and of centrin in the inducible *CNTROB* knockout. (A)** Immunofluorescence analysis of *iPLK4 KO* after 4 d induction. At this time point, the majority of cells (73.5% in *USP28Δ* RPE1 (*n* = 181) and 71% in *TRIM37Δ* RPE1 (*n* = 186) are acentrosomal, indicating loss of PLK4 function. No focal localization of PLK4 or centrobin is observed in acentrosomal *USP28Δ* RPE1 cells generated by inducible *PLK4* knockout. In acentrosomal *TRIM37Δ* RPE1 cells generated by inducible *PLK4 KO*, 11.8% have no condensate, whereas the rest have a condensate of varying size that contains both PLK4 and centrobin. Scale bars, 5 µm and 1 µm (insets). **(B)** Quantification of PLK4 and centrobin signal at condensates that persist after 4-d inducible *PLK4* knockout in *TRIM37Δ* RPE1 cells. All of the analyzed cells were acentrosomal, indicating sufficient loss of PLK4 function to prevent centriole duplication. Mean

and 95% CI are plotted on top of the individual values. Both PLK4 and centrobin are reduced at the condensates following PLK4 knockout (P values from unpaired *t* tests; **, P < 0.01). Note that the control (–Dox) data for condensates are the same as that shown in Fig. 1 G (analysis of this pair of *USP28Δ* and *TRIM37Δ* cell lines, ODCL0079 and ODCL0080, is reported in Fig. 1 G without Cas9 induction). The experiment shown in A and B was performed three times with similar results; data shown are from one experiment. **(C)** Centrin localization in mitotic control *USP28Δ* and *TRIM37Δ* cells following inducible knockout of *CNTROB*. The centrobin condensate is no longer detected in *TRIM37Δ* cells, but ectopic centrin foci (orange arrows) persist. Note that centrin is also present at centrosomes (white arrowheads). Scale bar, 5 µm. The experiment was performed three times with similar results; data shown are from one experiment.

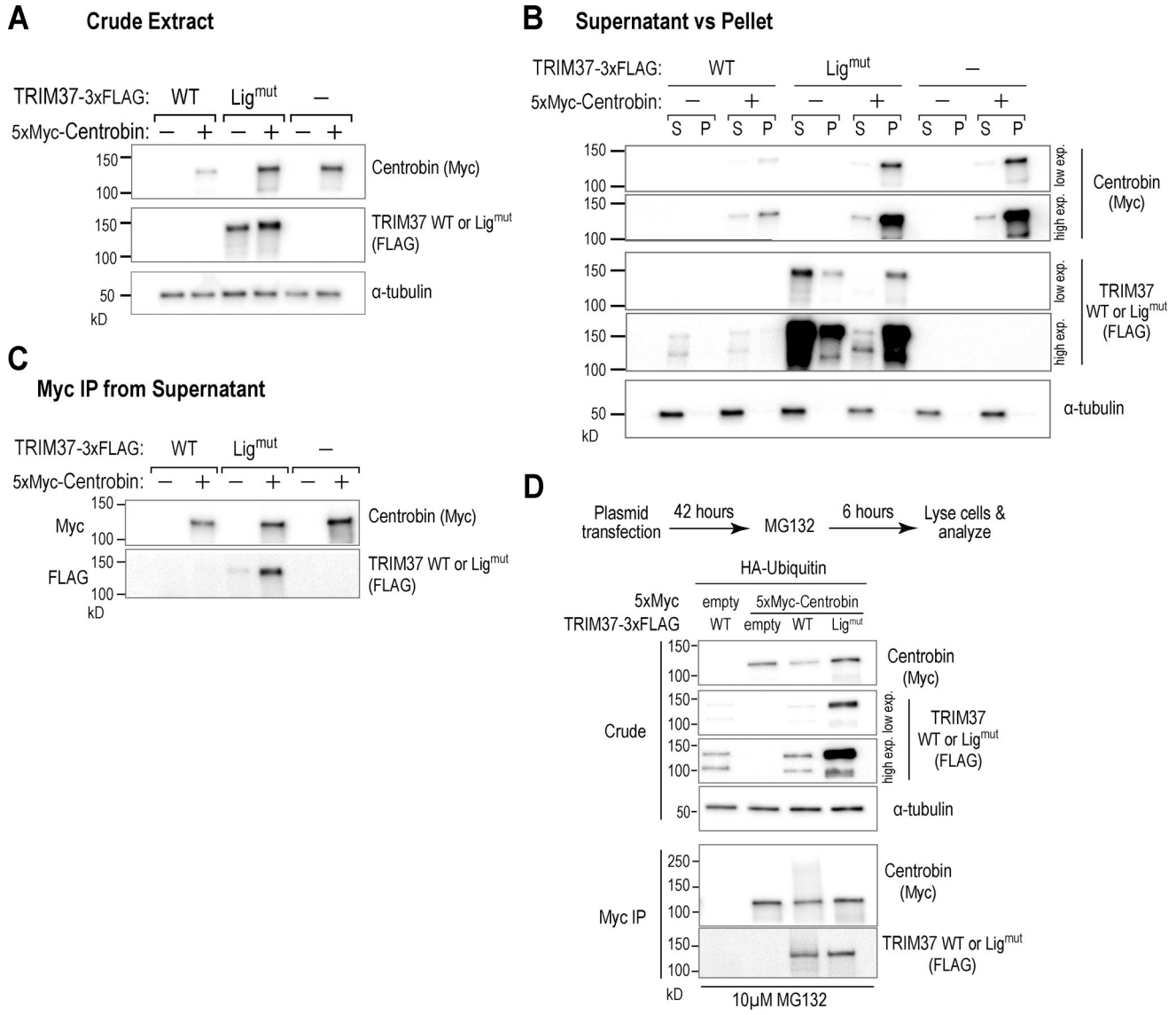

Figure S5. **Additional coexpression analysis of centrobin regulation by TRIM37. (A–C)** Results of an independent experiment assessing the effect of coexpressing TRIM37 (WT versus Lig^{mut}) and centrobin on centrobin levels (A) and relative solubility (B). In addition, interaction of Lig^{mut} TRIM37 with centrobin was analyzed (C). Quantification of levels and relative solubility is shown in Fig. 8 E. **(D)** Interaction of WT or Lig^{mut} TRIM37 with centrobin was analyzed in MG132-treated cells using the protocol schematized on the top. Anti-Myc and Anti-FLAG immunoblotting of anti-Myc immunoprecipitates is shown on the bottom. A plasmid encoding HA-ubiquitin was included in the coexpression. α-Tubulin serves as a loading control in A, B, and D.

Video 1. **Birth of a condensate.** Video shows *TRIM37Δ* RPE1 cells expressing Lig^{mut}-TRIM37-mNG, which localizes to condensates, and the microtubule-binding domain of MAP4 fused to mRuby2. The sequence initiates after cell division. The cell on the right inherited the condensate from the mother cell, and the cell on the left was born without a condensate. In both cells, the centrosome is held in the center of the frame. In the cell born without a condensate, there is a dramatic accumulation of Lig^{mut}-TRIM37-mNG at the centrosome to form a condensate that buds off near the end of the sequence. In the cell with the condensate, the condensate bounces in and out of the frame; although Lig^{mut}-TRIM37-mNG localizes to the centrosome, it does not accumulate there. 8 × 1.25–μm Z stacks were acquired every 5 min at 40× magnification. Image frames shown are maximum intensity projections at each time point. Playback is sped up 900× relative to real time. Elapsed time shown is in minutes, and scale bar is 10 μm.

Video 2. **Spindle assembly in control (*USP28Δ*) and *TRIM37Δ* RPE1 cells expressing the microtubule-binding domain of MAP4 fused to mRuby2.** Top: All control cells form bipolar spindles with a centrosome at each pole and divide in a bipolar fashion. Bottom: *TRIM37Δ* cells exhibit different fates: (left; bipolar) bipolar spindle forms with a centrosome at each pole, (middle; transient multipolar) multipolar spindle forms that resolves to a bipolar configuration with a centrosome at one pole and a centrosome and condensate at the other, and (right, dominant) multipolar spindle forms that resolves to a bipolar configuration with both centrosomes at one pole and the ectopic condensate at the other. 5 × 2–µm Z stacks were acquired every 4 min at 40× magnification. Image frames shown are maximum intensity projections at each time point. Playback is sped up 720× relative to real time. Elapsed time shown is in minutes, and scale bar is 10 µm.

Video 3. ***TRIM37Δ* RPE1 cells expressing an mNG fusion of WT or ligase mutant TRIM37 and a fusion of mRuby2 with the microtubule-binding domain of MAP4.** Top: All cells expressing WT TRIM37 (localizes to centrosomes) form bipolar spindles with a centrosome at each pole and divide in a bipolar fashion. Bottom: Cells expressing Lig^{mut} TRIM37 (localizes to centrosomes and the condensate) form an ectopic condensate and exhibit three different fates: (1) condensates do not nucleate microtubules and form bipolar spindles with a centrosome at each pole (right two cells; bipolar), (2) condensates nucleate microtubules and form multipolar spindles that resolve to a bipolar configuration with a centrosome at one pole and a centrosome and condensate at the other before division (left two cells; transient multipolar), and (3) condensates that nucleate microtubules and form multipolar spindles that divide in a multipolar configuration (middle cell, multipolar segregation). 8 × 1.2–µm Z stacks were acquired every 5 min at 40× magnification. Image frames shown are maximum intensity projections at each time point. Playback is 600× real time. Elapsed time is in minutes, and scale bar is 10 µm.

Video 4. **Chromosomes in control (*USP28Δ*) and *TRIM37Δ* RPE1 cells with and without induced centrobin knockout.** Chromosomes were labeled with SiR-DNA. In addition to bipolar divisions (left), chromosomes in *TRIM37Δ* cells exhibit an elevated frequency of transient multipolar configurations that resolve to a bipolar division (middle) and tripolar divisions (right). These aberrant configurations are not observed when CENTROB is also knocked out. 5 × 2–µm Z stacks were acquired every 5 min at 20× magnification. Image frames shown are maximum intensity projections at each time point. Playback is sped up 900× relative to real time. Elapsed time shown is in minutes, and scale bar is 10 µm.

Video 5. **Recovery after photobleaching of condensates in*TRIM37Δ* RPE1 cells expressing Lig^{mut}-TRIM37-mNG.** Condensates were photobleached at the indicated time point and recovery was monitored by collecting confocal fluorescence images at 100× magnification . A Z stack (17 sections at 0.2-µm intervals) was acquired every 1 min. Images shown are maximum intensity projections of the Z stacks at each time point. Playback is sped up 120× relative to real time. Elapsed time shown is in minutes. Scale bar is 1 µm.

Tables S1 and S2 are provided online as separate Word files. Table S1 lists the human cell lines used in this study. Table S2 lists the plasmids used in this study.